



Chair of Astronautics
Prof. Prof. h.c. Dr. Dr. h.c.
Ulrich Walter

Semester Thesis
Investigation of Transient Volatile Migration for the Lunar
Volatile Scout

RT-SA-2020/11

Author:
Alexander Smolka

Supervisor: M.Sc. Christian Gscheidle
Chair of Astronautics
Technische Universität München

Erklärung

Ich erkläre, dass ich alle Einrichtungen, Anlagen, Geräte und Programme, die mir im Rahmen meiner Semester- oder Masterarbeit von der TU München bzw. vom Lehrstuhl für Raumfahrttechnik zur Verfügung gestellt werden, entsprechend dem vorgesehenen Zweck, den gültigen Richtlinien, Benutzerordnungen oder Gebrauchsanleitungen und soweit nötig erst nach erfolgter Einweisung und mit aller Sorgfalt benutze. Insbesondere werde ich Programme ohne besondere Anweisung durch den Betreuer weder kopieren noch für andere als für meine Tätigkeit am Lehrstuhl vorgesehene Zwecke verwenden.

Mir als vertraulich genannte Informationen, Unterlagen und Erkenntnisse werde ich weder während noch nach meiner Tätigkeit am Lehrstuhl an Dritte weitergeben.

Ich erkläre mich außerdem damit einverstanden, dass meine Master- oder Semesterarbeit vom Lehrstuhl auf Anfrage fachlich interessierten Personen, auch über eine Bibliothek, zugänglich gemacht wird, und dass darin enthaltene Ergebnisse sowie dabei entstandene Entwicklungen und Programme vom Lehrstuhl für Raumfahrttechnik uningeschränkt genutzt werden dürfen. (Rechte an evtl. entstehenden Programmen und Erfindungen müssen im Vorfeld geklärt werden.)

Ich erkläre außerdem, dass ich diese Arbeit ohne fremde Hilfe angefertigt und nur die in dem Literaturverzeichnis angeführten Quellen und Hilfsmittel benutzt habe.

Garching, den _____

Unterschrift

Name: Alexander Smolka

Matrikelnummer: 03725319

Zusammenfassung

Diese Arbeit präsentiert den Aufbau und die Ergebnisse eines Simulationsmodels für den Lunar Volatile Scout (LVS) um die Massen- und Wärmetransportphänomene innerhalb von Mondregolith während der thermischen Extraktion von Volatilen zu untersuchen. Der Massentransport wird durch Desorption, Diffusion und Konvektion, der Wärmetransport durch Wärmeleitung, -strahlung, Konvektion und Wärmeerzeugung durch Desorption beschrieben. Die Phänomene wurden in COMSOL Multiphysics®[1] implementiert, wobei komplexe Zusammenhänge mittels externe Funktionen von der Software MATLAB [2] berechnet wurden. Die initialen Bedingungen sowie die Einstellungen des numerischen Lösers wurden durch vorbereitende Studien ermittelt. Der Hauptteil besteht aus einer Parameterstudie, welche die Auswirkungen von veränderlichen Wasseranteilen im Regolith sowie der Desorptionsenergie auf die thermale Extraktion untersucht.

Die Ergebnisse zeigen, dass das Verfahren funktioniert und die Anzahl an extrahierten Molekülen mit steigendem initialen Wasseranteil im Regolith sowie sinkender Desorptionsenergie zunimmt. Weiterhin werden die Einflüsse auf die Dampfdruck- und die Temperaturverteilung dargestellt. Mit zwei zusätzlichen Studien wurde der Einfluss von der Gaspermeabilität und den Faktoren der Kontakt-Wärmeleitung untersucht, wobei eine vernachlässigbare Abhängigkeit bezüglich der extrahierten Moleküle festgestellt wurde. Zuletzt wird eine Korrelationsstudie basierend auf den Ergebnissen eine Verifikationsstudie des thermalen Extraktionsverfahrens vorgestellt, wobei das vorhandene Simulationsmodel nicht korreliert werden konnte.



Abstract

This work presents the setup and workings of a simulation model for the LVS studying the mass and heat transfer mechanisms of volatile water inside of lunar regolith during a thermal extraction process. For the mass transfer desorption, diffusion, and convection, and for the heat transfer conduction, radiation, convection, and heat release through the desorption process was included. The physical behavior was implemented in COMSOL Multiphysics®[1] with external functions handled through its MATLAB [2] interface. Initial conditions as well as the numerical setup of the solver were derived through preliminary studies. The main work consists of a parameter study evaluating the effects of varying water ratios and desorption energies.

The results show that the extraction of volatile water is indeed possible and that the amount of extracted molecules increases with a higher water ratio and lower desorption energies of the soil. Additionally, the effects of the vapor pressure on the temperature distribution are presented. Two minor parameter studies looking at the varying gas permeability as well as solid conductance of the sample showed minimal effects on the total number of extracted volatiles, even though it did influence the pressure and temperature distribution in the soil. A correlation study featuring an experimental setup to confirm functionality of the thermal extraction method is presented, though the current version of the simulation model could did not correlate.



Contents

1 INTRODUCTION	1
2 MATHEMATICAL MODEL	3
2.1 Mass Transfer	3
2.1.1 Sorption Mechanisms	3
2.1.2 Mass Transport Mechanisms	5
2.2 Heat Transfer	8
2.2.1 Thermal Conductivity	8
2.2.2 Convection	11
2.2.3 Sorption Energy	11
3 NUMERICAL MODEL AND COMPUTATIONAL SETUP	12
3.1 Implementation	12
3.2 Geometry Model	12
3.3 Boundary Conditions	13
3.4 Initial Conditions	16
3.5 Model and Solver Setup	20
3.5.1 Mesh Study	20
3.5.2 Domain Study	21
3.5.3 Timestep Study	22
4 RESULTS	24
4.1 Baseline	24
4.2 Water Ratio Study	27
4.3 Desorption Energy Study	29
4.4 Additional Studies	30
4.4.1 Gas Permeability	31
4.4.2 Solid Thermal Conductance	31
5 CORRELATION STUDY	34
6 CONCLUSION AND OUTLOOK	36
BIBLIOGRAPHY	36
APPENDIX	40

List of Figures

Fig. 1–1:	Schematic view of the LVS.	2
Fig. 2–1:	Residence time of water molecules adsorbed on lunar regolith	4
Fig. 2–2:	Bulk density and porosity of the lunar regolith.	6
Fig. 2–3:	Thermal conductivity of lunar regolith.	8
Fig. 2–4:	Thermal conductivity; comparison.	11
Fig. 3–1:	CAD Model and discretized geometric model of the LVS.	13
Fig. 3–2:	Boundary conditions.	14
Fig. 3–3:	Sketch of the initial conditions study model.	15
Fig. 3–4:	Convergence graph of the initial conditions study.	16
Fig. 3–5:	Initial conditions T .	17
Fig. 3–6:	Initial conditions c_d .	18
Fig. 3–7:	Initial conditions c_a .	19
Fig. 3–8:	Mean squared errors of the mesh study.	21
Fig. 3–9:	Mean squared errors of the domain study.	22
Fig. 3–10:	Mean squared errors of the timestep study.	23
Fig. 4–1:	Results of the baseline simulation.	25
Fig. 4–2:	Water ratio study; molar flux.	26
Fig. 4–3:	Water ratio study; average pressure.	27
Fig. 4–4:	Water ratio study; temperature distribution.	28
Fig. 4–5:	Desorption energy study; molar flux.	30
Fig. 4–6:	Desorption energy study; average pressure.	31
Fig. 4–7:	Desorption energy study; temperature distribution.	32
Fig. 4–8:	Gas permeability study; average pressure.	33
Fig. 4–9:	Gas permeability study; temperature distribution difference.	33
Fig. 5–1:	Results of the thermal extraction verification test with a sample.	35
Fig. A-1:	Thermal conductivity; comparison.	41
Fig. A-2:	Thermal conductivity ratios; Apollo 16 Sample 68501 Fit.	42
Fig. A-3:	Thermal conductivity ratios; Basic Rock.	42
Fig. A-4:	Thermal conductivity ratios; Metamorphic Rock.	43
Fig. A-5:	Thermal conductivity ratios; Acid Rock.	43
Fig. A-6:	Thermal conductivity ratios; Limestone.	44
Fig. A-7:	Thermal conductivity ratios; Ultrabasic Rock.	44
Fig. B-1:	Sketch of the LVS enclosure.	46

List of Tables

Tab. 2–1:	Nominal lunar conditions.	5
Tab. 2–2:	Gas permeabilities for different materials.	7
Tab. 2–3:	Solid conductance coefficients for different rock types.	9
Tab. 4–1:	Parameters of the baseline setup.	24
Tab. 4–2:	Most important numerical solver settings.	25
Tab. 4–3:	Values for the water ratio study.	26
Tab. 4–4:	Values for the desorption energy study.	29
Tab. B-1:	Resulting view factors.	46

Symbols and Constants

Symbol	Unit	Description
b	Pa	Klingenberg parameter
c, c_d, c_a	mol/m ³	concentration, desorbed/adsorbed species
c_{mol}	m ³ / s	molar conductivity
c_p	J / (kg · K)	specific heat capacity
d_g	m	effective diameter of gas molecule
d_v	m	mean void diameter
D	m ² /s	diffusion coefficient
e, \bar{e}	-	relative error / mean squared error
E	1 / m	extinction coefficient
E_d	eV	desorption energy
f	mol/(m ³ · s)	source term of the mass transfer
F_{ell}	-	shape factor
g	m / s ²	gravitational acceleration
$hgrad$	-	mesh growth rate
$hmax$	m	maximum size of mesh element
$F_{i \rightarrow j}$	-	view factor
k	W / (m · K)	thermal conductivity
k_d	1 / s	rate constant of the desorption process
$k_{g,a}$	m ²	apparent gas permeability
Kn	-	Knudsen number
n	-	refractive index
\dot{n}	mol / s	molar flux
p	Pa	pressure
\dot{q}	W / m ²	heat flux density
\dot{Q}	W	heat flux
r, z	m	radius and depth coordinate
t	s	time
T	K	temperature
u	m/s	conservative convection coefficient / darcy velocity
\bar{v}	m/s	mean thermal velocity
V	m ³	volume
Y	Pa	Young's modulus

Symbol	Unit	Description
λ	m	mean free path
μ	kg · m / s	dynamic viscosity
ν	-	Poisson ratio
Φ	-	porosity
Ψ	wt.%	water ratio
ρ	kg / m ³	density
τ	-	tortuosity
Θ	-	surface coverage

Constant	Value	Unit	Description
h	6.6261×10^{-34}	J · s	Planck's constant
k_B	1.3807×10^{-23}	J/K	Boltzmann constant
M_{H2O}	18.01528×10^{-3}	kg/mol	molecular weight of water
N_A	6.02214×10^{23}	1/mol	Avogadro's constant
R	8.3144598	J/(K · mol)	universal gas constant
σ	5.670374×10^{-8}	W/(m ² · K ⁴)	Stefan-Boltzmann constant

Acronyms

CAD Computer-Aided Design

DBC Dirichlet Boundary Condition

LVS Lunar Volatile Scout

PDE Partial Differential Equation

TUM Technical University of Munich

1 Introduction

Lunar resources are considered the key for future, long-duration explorations of the Moon. Its regolith contains significant quantities of oxides, metals, and highly volatile elements including water [3]. Once data suggested that water exists in cold traps at the lunar poles, the latter has become the focus of the scientific interest. Since it is assumed that the regolith temperatures at sample sites are at about 120 K to 150 K, the volatile water can be present as physically (loosely) and chemically (strongly) bound species [4]. Missions like the Russian Luna-27 aim to further explore the existence of volatile water on the Moon[5].

In-situ extraction of the volatile components from regolith involves thermal processing and strongly depends on the heat and mass transfer inside of the lunar soil. While these processes are influenced by a large number of physical properties like the porosity and the tortuosity of the sample, the respective gas density, and its temperature and pressure, the description of the interaction between heat and gas transfer and sorption mechanisms poses to be a difficult problem.

The LVS, a novel soil sampling and analysis instrument developed jointly by the Institute of Astronautics at the Technical University of Munich (TUM), OHB Systems AG, and the Open University, aims to shed light on the behavior of the volatiles at the lunar poles [6]. It is an in-situ tool to access and characterize lunar volatiles consists of two main sections, the hollow drill acting as a sampler, and the attached volatile analyzer, a mass spectrometer, see Fig. 1–1. As shown in the figure, the LVS will be inserted into the lunar soil to a depth of about 100×10^{-3} m to 150×10^{-3} m. Once inserted, the heating rod in the middle of the instrument will continuously heat up the surrounding regolith. With sufficiently high temperatures enough energy has accumulated to break the bond of the volatile with its respective particle, which means that the volatile will desorb and diffuse through the soil. A mass spectrometer will analyses those volatiles that travelled upwards to the top of the instrument.

This approach to analyze the lunar soil comes with a set of challenges the LVS has to tackle. It is based on a unique and untested concept with an open enclosure for the sample, which has to be accounted for during all experiments using the instrument.

To analyze the thermal extraction of volatiles bears the problem of an accurate description of the temperature distribution. Due to the extremely low and non-linear thermal conductivity of the lunar regolith, it is difficult to predict how the heat is spreading through the soil [7].

The current study uses the LVS as baseline for a computational model to further analyze the extraction mechanism of water in lunar regolith. With the software COMSOL Multiphysics and MATLAB, a combined model for the heat and mass transfer as well as the desorption mechanism, was developed based on the model by *Reiss* [7]. The

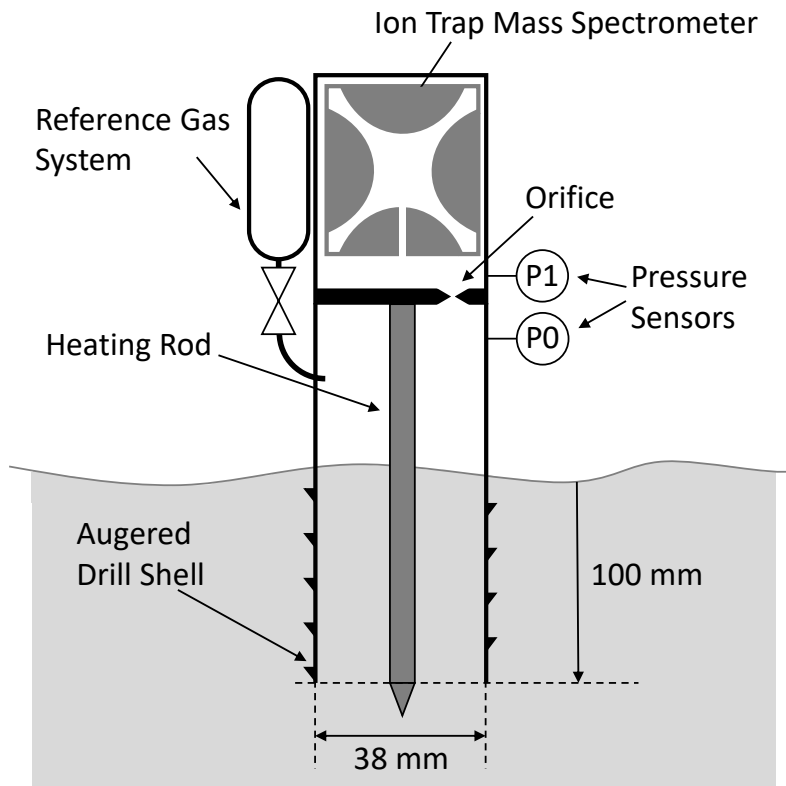


Fig. 1–1: Schematic view of the LVS.

physics were modelled in COMSOL Multiphysics using Partial Differential Equation (PDE) in coefficient form, based on the diffusion-convection equation. The evaluation of the temperature and pressure dependent thermal conductivity and gas diffusivity at every timestep was done externally in MATLAB.

The main questions this study aims to answer are to describe the thermal behavior and distribution of both the instrument as well as the surrounding regolith during the extraction process and to analyze the mass fluxes over the regolith surface as well as the internal regolith boundary leading into the enclosure of the LVS.

This study is structured so that first the mathematical model of the simulation is explained. The underlying PDE's for both the heat and the mass transfer are presented as well as the physical properties considered in the simulation. Second, the numerical model is introduced. This includes the numerical implementation of the physics and the LVS as well as the preparatory studies conducted prior to the main analysis. For the latter, a parameter study for several different physical parameters and boundary conditions is presented. A correlation study based on experiments done at the Chair of Astronautics at the TUM follows [6]. The work concludes with a discussion of the presented results as well as an outlook on further studies regarding the thermal extraction of lunar volatiles.

2 Mathematical Model

This chapter introduces and explains the implemented mathematical background for the setup of the simulation model. Firstly, the mathematical behavior of the mass transfer mechanisms is covered. Secondly the heat transfer mechanisms are presented in more detail.

2.1 Mass Transfer

The combined PDE for the mass transfer is

$$\frac{\partial c}{\partial t} + \nabla \cdot (-D \nabla c - uc) = f \quad (2-1)$$

with the concentration c , the diffusion coefficient D , the conservative convection coefficient u , and the source term f . In the following sections, each part of Eq. 2–1 will be discussed in more detail, starting with the sorption mechanisms that govern the source term f , followed by transport mechanisms which explain the diffusion coefficient D as well as the conservative convection coefficient u .

According to this PDE, the concentration c depends on various parameters and variables. It is a function of the time and the spatial coordinates, and due to the temperature and pressure dependency of the diffusion coefficient D also a function of the temperature and itself: $c = f(t, \underline{x}, T, c)$.

2.1.1 Sorption Mechanisms

The two sorption mechanisms are the desorption and the adsorption. In the context of this work, the former describes how the bond of volatile water molecules with lunar regolith is broken, while the latter focuses on the inverse reaction where new bonds of the molecules with the particle surfaces are formed. In order to reduce the complexity and non-linearity of the problem, only the desorption process was included in the simulation model of this work, while for the adsorption an approach is given in the appendix.

2.1.1.1 Desorption

The rate with which adsorbed molecules are desorbed from their particle's surface can be described with the Polanyi-Wigner equation [7]:

$$\frac{d\Theta}{dt} = -k_d \Theta^n \quad (2-2)$$

with the surface coverage Θ , which is the ratio of occupied sites on the particle surface, the rate constant k_d , and the order of desorption n with $n = 1$ in the case for the

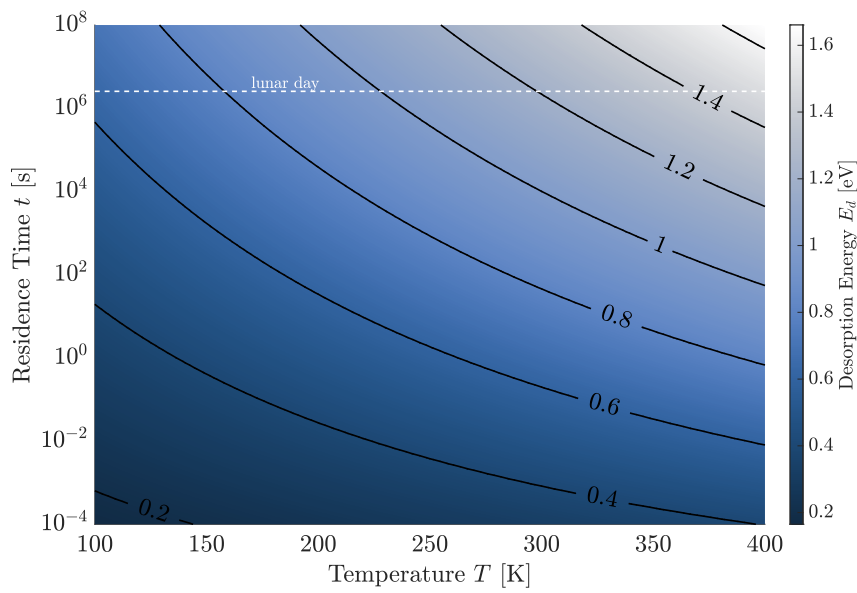


Fig. 2–1: Residence time of water molecules adsorbed on lunar regolith with varying desorption energies E_d .

desorption of molecular water [8]. The rate constant is described by the Arrhenius equation [9, 7]:

$$k_d = \frac{k_B T}{h} \cdot \exp\left(\frac{-E_A}{RT}\right) = \frac{k_B T}{h} \cdot \exp\left(\frac{-E_d}{k_B T}\right) \quad (2-3)$$

with the Boltzmann constant k_B , the Planck constant h , the universal gas constant R , the temperature T , the free enthalpy of activation E_A , and the desorption energy E_d . The unit of k_d depends on the order of the reaction and is $[s^{-1}]$, which resembles a frequency, for a first-order process.

The inverse of the rate constant can be interpreted as the residence time of water molecules adsorbed on lunar regolith. Figure 2–1 shows the residence time $t = k_d^{-1}$ for different desorption energies E_d as a function of the temperature. The dashed line at $t \approx 29.5$ d indicates the length of one lunar day. The lower and upper limit of the desorption energies shown in the figure correspond to the minimum desorption energy for water ice clusters of $E_d = 0.45$ eV [8], and the maximum desorption energy for strongly chemisorbed water of $E_d = 1.2$ eV [10]. Reportedly, less than 10% of the bindings have desorption energies of more than 0.9 eV [7].

As indicated in Fig. 2–1, low desorption energies result in short residence times. Even at temperatures as low as 175 K the desorption can take place in less than one second. This behavior changes drastically for stronger bonds, where the residence times can exceed the duration of an entire lunar day at temperatures of about 300 K.

2.1.1.2 Adsorption

While a complete description of the mass transport would include both sorption processes, the simulation model for this work only implemented the desorption. This decision was made based on several factors:

1. due to the constant heating it is expected that once temperature are high enough for meaningful desorption to take place, the desorption will always be dominant over the resorption,
2. the additional non-linearity coming from a possible implementation of the adsorption results in numerical difficulties and instabilities during the solving process.

Nevertheless, an approach to modelling the resorption process is given in App. C.

2.1.2 Mass Transport Mechanisms

This section covers the main transport mechanisms for the desorbed volatiles. First, the diffusion process is explained, second the convective transport is presented.

2.1.2.1 Diffusion

The most important value that describes the diffusion process of the volatiles in a porous medium is the Knudsen number

$$Kn = \frac{\lambda}{d_v} \quad (2-4)$$

with the mean free path λ and the diameter of the void spaces between the particles d_v . The former can be calculated as

$$\lambda = \frac{k_B T}{\sqrt{2} p \pi d_g^2} \quad (2-5)$$

with the Boltzmann constant k_B , the temperature T , the pressure p , and the effective diameter of a gas molecule d_g .

The Knudsen number is used to differentiate between ordinary and Knudsen diffusion. While there is no exact definition of the boundary between these two mechanisms it is commonly said that for $Kn \ll 0.1$, where the void spaces are much larger than the mean free path, ordinary diffusion is the dominating diffusion process. Accordingly, for $Kn \gg 1..10$ Knudsen diffusion dominates [7].

At normal lunar conditions, see Tab. 2–1, the environment pressure and temperature lead to a Knudsen number above 10 and, thus, to a Knudsen diffusion governed transport. If through external heating the pressure and temperature would change however, transport mechanisms in the transition region could occur. This makes it necessary to calculate the diffusivity dynamically during the volatile extraction process [7].

Tab. 2–1: Nominal lunar conditions [11].

Property	Value
Diurnal Temperature Range	95 K to 390 K
Surface Pressure	3×10^{-15} bar to 9×10^{-15} bar

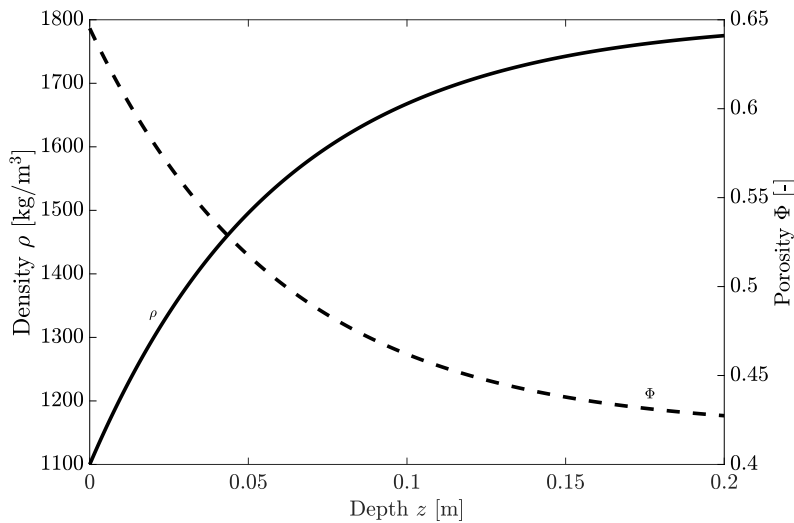


Fig. 2–2: Bulk density and porosity of the lunar regolith [3].

Both ordinary and Knudsen diffusion can be described by Fick's first law

$$J_D = -D \nabla c \quad (2-6)$$

with the diffusion coefficient D and the concentration gradient ∇c . The former can be calculated using the mean thermal velocity \bar{v} with the universal gas constant R and the molecular weight M , which leads to

$$D_O = \frac{\lambda}{3} \bar{v} \quad \text{or} \quad D_K = \frac{d_v}{3} \bar{v} \quad (2-7)$$

with

$$\bar{v} = \sqrt{\frac{8RT}{\pi M}} \quad (2-8)$$

for ordinary and Knudsen diffusion, respectively [12].

Since the Eqs. (2-7) are only valid for parallel cylindrical voids leading to an unobstructed path for the diffusion [7], the effective diffusivity has to be calculated by taking the porosity Φ and tortuosity τ into account. The former depends on the densities of the bulk and particle, ρ_{bulk} and $\rho_{particle}$ respectively:

$$\Phi = \frac{V_v}{V} = 1 - \frac{\rho_{bulk}}{\rho_{particle}}. \quad (2-9)$$

with the void and the total volume, V_v and V , respectively. Since the density of the lunar soil depends on the depth [3] according to

$$\rho_{bulk} = 1800 \frac{kg}{m^3} - 700 \frac{kg}{m^3} \cdot \exp\left(-\frac{z}{0.06 m}\right) \quad (2-10)$$

with the depth z . Both the porosity and the density are shown in Fig. 2–2 leading up to a depth of 0.2 m. While the density increases with higher depths, the porosity decreases.

Tab. 2–2: Gas permeabilities lunar soil and different simulants.

Material	Value [m ²]	Reference
Lunar Soil	$1..7 \times 10^{-12}$	<i>Choate et al. [14]</i>
JSC-1A	$3 \times 10^{-13} .. 2 \times 10^{-12}$	<i>Toutanji et al. [15]</i>
NU-LHT	$9 \times 10^{-14} .. 1 \times 10^{-12}$	<i>Toutanji et al. [15]</i>

This results in the effective diffusion coefficients for ordinary and Knudsen diffusion as

$$D_{O,eff} = \frac{\Phi}{\tau} \cdot D_O \quad (2-11)$$

and:

$$D_{K,eff} = \frac{\Phi}{\tau} \cdot D_K. \quad (2-12)$$

In order to combine the two diffusive mechanisms, the effective diffusion coefficients can be linked according to the "resistance in series" approach [13]:

$$\frac{1}{D_{eff}} = \frac{1}{D_{O,eff}} + \frac{1}{D_{K,eff}} \quad (2-13)$$

2.1.2.2 Convection

Another part of the mass transfer is the convective flux of the volatiles through the porous medium. This transport can be described as

$$J_C = c \cdot u = -c \frac{k_{g,a}}{\mu} \nabla p \quad (2-14)$$

with the concentration c , the darcy velocity

$$u = -\frac{k_{g,a}}{\mu} \nabla p, \quad (2-15)$$

the apparent gas permeability $k_{g,a}$, the dynamic viscosity μ , and the pressure gradient ∇p [16]. In this form gravity effects are assumed to be negligible compared to the applied pressure gradient.

In order to account for the gas saturation, which is the fraction of the void volume occupied by the gas, and slip effects inside of the porous regolith, which increases the apparent permeability, its value has to be adjusted with the help of the Klingenberg parameter b [16]

$$k_{g,a} = k_{g,e} \left(1 + \frac{b}{\bar{p}} \right) \quad (2-16)$$

with the average pressure \bar{p} . Values for the gas permeability of lunar soil were determined during firing tests of the Surveyor 5 Vernier engine [7]. Table 2–2 lists values for the permeability for both lunar regolith as well as different regolith simulants.

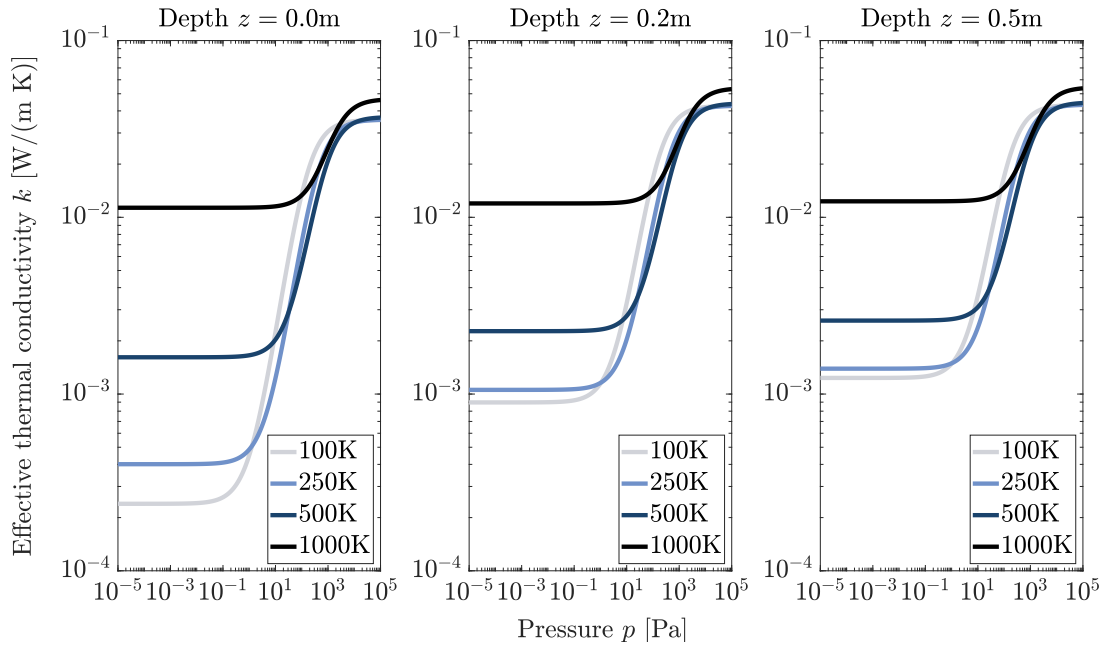


Fig. 2–3: Effective thermal conductivity k of lunar regolith for different depths z as a function of the temperature and the pressure.

2.2 Heat Transfer

The general version of the heat transfer PDE, based on a conventional diffusion-convection equation, is

$$(\rho c_p)_{sg} \frac{\partial T}{\partial t} + \nabla \cdot \left(-k \nabla T - (\rho c_p)_g u T \right) = Q \quad (2-17)$$

with the density ρ , the specific heat capacity c_p , the temperature T , the thermal conductivity k , the convective term u , and a source term Q . The index $(\bullet)_{sg}$ denotes the solid-gas mixture, where the product of the density and the specific heat constant can be written as

$$(\rho c_p)_{sg} = (1 - \Phi) \rho_s c_{p,s} + \Phi \rho_g c_{p,g} \quad (2-18)$$

with the respective values for the solid $(\bullet)_s$ and the gas $(\bullet)_g$ which are connected with the porosity Φ .

2.2.1 Thermal Conductivity

For the porous lunar soil several heat transfer mechanisms need to be considered [7]:

- physical contact conduction k_{sc} ,
- radiation between the particles k_{rad} ,
- conduction through the gas in between the particles k_{gas} , and
- coupling of solid and gas conduction k_{sg} .

Tab. 2–3: Solid conductance coefficients for different rock types.

C_1	C_2	Description
0.5	0.38	Apollo 16 sample 68501 fit
474.0	1.18	basic rock
750.0	0.75	metamorphic rock
807.0	0.64	acid rock
1073.0	0.13	limestone
1293.0	0.73	ultrabasic rock

For the effective thermal conductivity k , a linear connection of the listed mechanisms can be assumed [17]:

$$k = k_{sc} + k_{rad} + k_{gas} + k_{sg}. \quad (2-19)$$

The first mechanism considers the contact area between the particles and, thus, depends mostly on the mechanical properties of the regolith [17]:

$$k_{sc} = 3.44 \cdot (1 - \Phi)^{\frac{4}{3}} \left(\frac{1 - \nu^2}{Y} \right)^{\frac{1}{3}} k_s p_s^{\frac{1}{3}} \quad (2-20)$$

with the Poisson ratio ν , Young's modulus Y , the thermal conductivity of the solid material k_s , and the pressure or load on the particle p_s . The load can be calculated by integrating the weight of the soil above:

$$p_s = g \cdot \int_0^z \rho_s dz = g \cdot \left(1800 \frac{kg}{m^3} \cdot z + 42 \frac{kg}{m^2} \cdot \exp\left(-\frac{z}{0.06 m}\right) \right) \quad (2-21)$$

with the density ρ_s and the gravitational acceleration g . The conductivity of the solid material can be evaluated using the general equation for thermal conductivity of rocks [18, 19]:

$$k_s = \frac{C_1}{T + 76.85} + C_2 \quad (2-22)$$

which features two fitting parameters C_1 and C_2 . These two factors depend on the rock type with Tab. 2–3 showing a few common combinations as well as a fit for the Apollo 16 sample 68501 [7]. The latter was used in this study to evaluate the heat transport in the simulation of lunar soil. A closer analysis of the effects of the two factors C_1 and C_2 can be found in App. A. Generally, the thermal conductivity k_s of the lunar soil fit parameters is up to two orders of magnitudes lower than the other combinations, especially in the low temperature and low pressure region. It is assumed that this effect is due to the high agglutinate content in the sample, which is glassy breccia with vesicles that formed by melting and outgassing of solar wind implanted particles [7, 20].

The radiative term k_{rad} depends on the real part of the complex effective refractive index n :

$$n^2 = n_f^2 \cdot \left(1 + \frac{3(1 - \Phi) \frac{n_s^2 - n_f^2}{n_s^2 + 2n_f^2}}{1 - (1 - \Phi) \frac{n_s^2 - n_f^2}{n_s^2 + 2n_f^2}} \right) \quad (2-23)$$

with the refractive indices of the fluid n_f and the solid n_s [17, 7]. Now the conduction can be calculated as:

$$k_{rad} = \frac{16\sigma n^2}{3E} \cdot T^3 \quad (2-24)$$

with the Stefan-Boltzmann constant σ , the temperature T , and the so called extinction coefficient E . The latter was tuned to fit the Apollo 16 data for the measured radiative thermal conduction.

The gas conductivity increases with a decreasing Knudsen number (see Eq. (2-4)) following the effects from the Smoluchowski effect [21]:

$$k_{gas} = \frac{k_{gas,0}}{1 + 2\beta \cdot Kn} \quad (2-25)$$

with the thermal conductivity of the gas at atmospheric pressure $k_{gas,0}$ and the gas specific constant $\beta = 1.41$ for water [22]. Thus, the equation above approaches the ordinary gas conduction at pressures close to atmospheric [7].

The final term k_{sg} originates from the interaction between the solid and the gas. In order to evaluate this contribution to the overall conductivity, the model by *Swimm et al.* [23] can be used. This approach discretizes the contact area using 1000 hollow cylinders and an additional shape factor to contribute to the deviation from perfectly spherical contact zones. Thus, the term can be written as:

$$k_{sg} = (1 - \Phi_{uc}) \cdot \frac{2r}{r^2\pi} \cdot \sum_{i=1}^{1000} \left(\frac{h_{g,i}}{k_{gas,i}A_i} + \frac{h_{s,i}}{k_s A_i} \right)^{-1} \quad (2-26)$$

with the particle radius r . All additional factors can be calculated as follows:

$$\Phi_{uc} = \frac{1}{2}(3\Phi - 1), \quad (2-27)$$

$$a = \frac{d}{2} F_{ell}^{-\frac{1}{3}}, \quad (2-28)$$

$$b = \frac{d}{2} F_{ell}^{\frac{2}{3}}, \quad (2-29)$$

$$h_{s,i} = 2r - 2b \cdot \left(1 + \sqrt{1 - \left(\frac{i}{a} \frac{r}{1000} \right)^2} \right), \quad (2-30)$$

$$h_{g,i} = 2r - h_{s,i}, \quad (2-31)$$

$$A_i = \pi \left(\frac{r}{1000} \right)^2 \cdot (2i - 1). \quad (2-32)$$

Comparing the particle shapes of lunar soil samples and the simulant JSC-1A, the shape factor $F_{ell} = 0.6$ can be assumed [17]. The resulting thermal conductivity for different materials listed in Tab. 2-3 is shown in Fig. 2-4. A more detailed discussion about the results shown in the figure are presented in App. A.

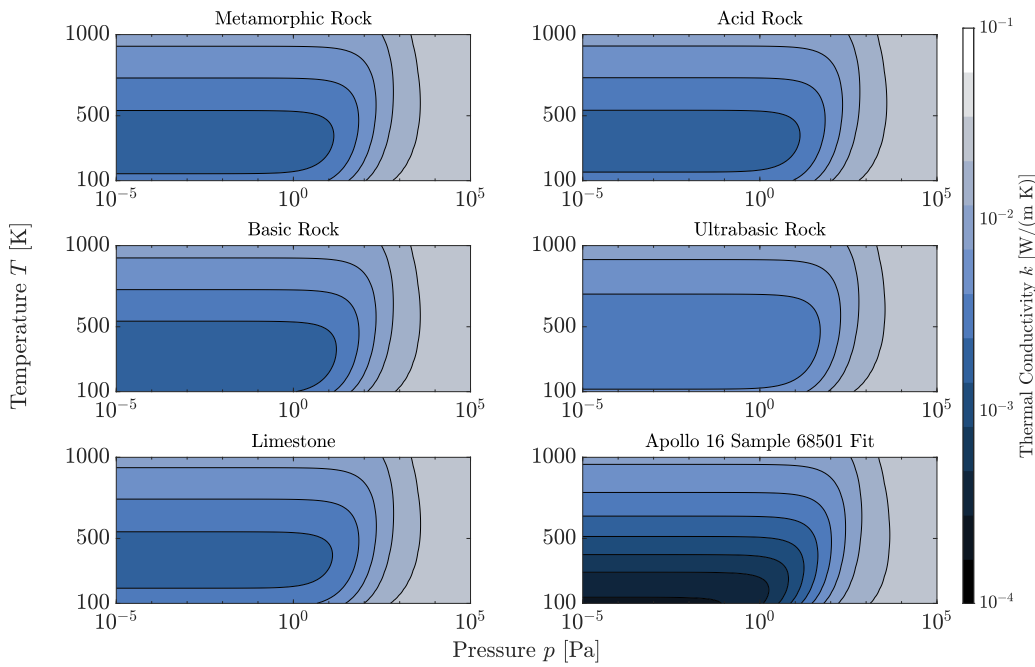


Fig. 2–4: Comparison of the thermal conductivity as a result of changing factors C_1 and C_2 of the solid conductance term.

2.2.2 Convection

Similar to the convection discussed for the mass transfer in Sec. 2.1.2.2, this heat transport mechanism can be described with the darcy velocity, see Eq. (2–15). This velocity can subsequently be used in Eq. (2–17).

2.2.3 Sorption Energy

The desorption of the volatiles requires energy which is introduced into the lunar soil through heating. As discussed in Sec. 2.1.1.1, the rate of desorption can be described by the rate constant k_d , which in turn depends on the temperature T and the desorption energy E_d , see Eq. (2–3). With a lower required desorption energy, the rate constant exponentially increases, since less energy is needed to break the volatile's bond to its particle. In order to describe the total heat sink due to the used energy, the rate constant as well as the desorption energy can be used:

$$Q = -k_d \Theta c N_A E_d \quad (2-33)$$

with the concentration c , the surface coverage Θ , and the Avogadro constant N_A . Similar to the mass transport mechanisms, the adsorption process was not included in the description since continuous heating of the soil during the simulation will not result in a meaningful contribution of the adsorption.

3 Numerical Model and Computational Setup

This chapter provides an overview about the implementation of the presented physical behaviors of the thermal and the mass transport mechanisms into the simulation model. It features a short presentation of the geometry and its discretization and shows the boundary and initial conditions, with the latter being based on an entire one dimensional initial conditions study. Afterwards, further preliminary studies for the mesh and domain size as well as the numerical solver setup including the resulting simulation setup are presented.

3.1 Implementation

The PDE's presented in the previous section were implemented into the simulation model using COMSOL Multiphysics Coefficient Form PDE physics nodes with a total of three dependent variables. These variables are the temperature T , the adsorbed volatile water concentration c_a , and the desorbed water concentration c_d . While the first controls the thermal transport mechanisms, the last two jointly describe the mass transfer in the regolith domain. The desorbed species controls the water vapor pressure and concentration, and, thus, the diffusion inside of the regolith, while the adsorbed species acts as a reservoir that is accessed through the desorption mechanism. Computationally, these two quantities are linked through the source term f of Eq. (2–1):

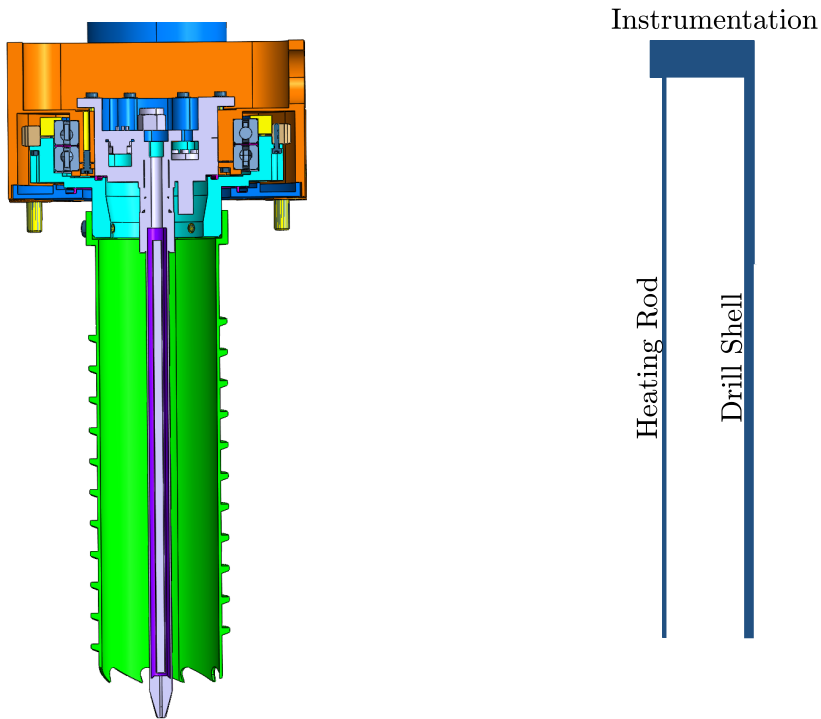
$$\frac{\partial c_d}{\partial t} + \nabla \cdot (-D \nabla c_d - u c_d) = k_d c_a, \quad (3-1)$$

$$\frac{\partial c_a}{\partial t} = -k_d c_a. \quad (3-2)$$

Furthermore, the thermal conductivity k and the diffusion coefficient D are both depending on the temperature and the pressure of the water vapor, as seen in the previous section. The complex mathematical description was implemented as MATLAB functions and then included in the simulation model in COMSOL Multiphysics [7].

3.2 Geometry Model

The simulation model approximates the LVS using a 2D-axisymmetric geometry in order to decrease the computational effort. While the instrument itself consists of a multitude of parts, only three geometric interfaces were identified to influence the results significantly. Figure 3–1 shows both the Computer-Aided Design (CAD) model view on the left side as well as the discretized version of the geometry on the right side. The cut view of the CAD model reveals the heating rod placed in the center of the drill shell and the entire instrument. While these two parts were implemented directly into the simulation model, the remaining parts of the LVS are simply approximated by a connecting bar at the top of the heating rod and drill shell, called instrumentation. While the heating rod is used as an interface to introduce heat into the regolith, the drill shell



(a) Cut view of the CAD model of the LVS. (b) 2D-Axisymmetric geometric model of the LVS' geometry.

Fig. 3–1: CAD model and discretized geometric model of the LVS.

acts as a hard boundary for the mass transport of the volatiles during the simulation. The connector is used to thermally connect the other two parts, as well as provide further interfaces for boundary conditions.

3.3 Boundary Conditions

Figure 3–2 shows a complete view of the boundary conditions introduced to the simulation for both the LVS and the lunar regolith. The ones for the instrument are purely thermal since no mass transport was modelled for the domains other than the regolith. With the constant temperature at the top of the connector, the connection to the rest of the instrument is modelled, which shall have a constant temperature around 0 °C at all times to prevent the sensors and other sensitive equipment from being damaged. \dot{Q}_{Heater} provides a constant heat source for the lower part of the heater. The remaining boundary conditions are used to implement radiative heat exchange between the LVS, the soil, and the environment. The calculation of the respective view factors for the void enclosure of the instrument can be found in the App. B.

As with the LVS, the lunar regolith was implemented as a 2D-axisymmetric domain in the simulation model. While the geometry is a simple cylinder with a certain radius and height, the instrument is inserted into the soil for 100 mm, which creates a pocket of regolith in between the drill shell and the heater. Since the behavior of this patch of regolith is of increased interest, it was implemented as its own domain, referred to as the regolith inside of the LVS' enclosure.

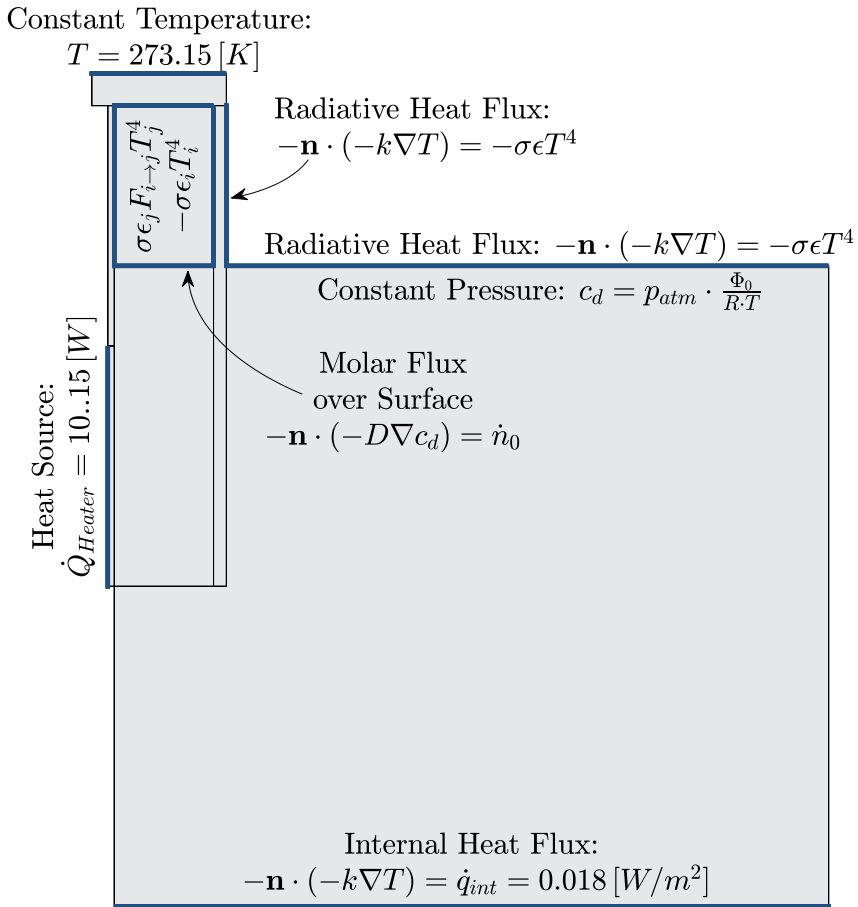


Fig. 3–2: Overview of the boundary conditions applied to the 2D-axisymmetric model implemented in COMSOL Multiphysics. The size of the geometry is not to scale.

The boundary conditions were already shown in Fig. 3–2, while this time said conditions apply to both the thermal transport and the mass transport inside of the domain of the regolith. For the surface of the regolith outside of the enclosure both a thermal condition for the radiative heat flux emitted as well as a Dirichlet Boundary Condition (DBC)s for the desorbed species were implemented. The latter takes the minimal atmospheric pressure of the Moon into account, which prevents the partial water vapor pressure and, thus, the c_d to drop down to zero, improving the stability of the simulation. The lower boundary of the regolith features a constant heat flux to model the internal heat coming from the lunar core as a result of its radioactivity.

The surface of the regolith inside of the LVS' enclosure is also equipped with two boundary conditions, the thermal one modelling the radiative heat exchange between the surfaces of the enclosure, and the molar one for the mass flux over the surface and, thus, through the mass spectrometer of the instrument. While the latter part is not included in the geometry representation, it does have a significant influence on the behavior of the volatile water. The gaseous phase does not only accumulate in the enclosure once it left the regolith domain, it also travels through three orifices into the surrounding atmosphere at p_{atm} , which models the fluid mechanical behavior of the gas flowing through the mass spectrometer.

This model is based on previous investigation of the LUVMI instrument [24], which uses the molar conductivity

$$c_{mol} = \bar{v} \cdot \frac{A}{4} \quad (3-3)$$

with the thermal velocity \bar{v} , and the orifices size A to calculate the molar flux through said orifice:

$$\dot{n} = c_{mol} \cdot \frac{p_2 - p_1}{R \cdot T}. \quad (3-4)$$

The path of the gas exiting the regolith can be described by three volumes divided by the three orifices with the last one leading to the atmosphere. Using Eq. (3-4) for every volume, i.e. each orifice, leads to

$$\dot{n}_0 = c_{mol,0} \cdot \frac{p_0 - p_1}{R \cdot T_0}, \quad (3-5)$$

$$\dot{n}_1 = c_{mol,1} \cdot \frac{p_1 - p_2}{R \cdot T_1}, \quad (3-6)$$

$$\dot{n}_2 = c_{mol,2} \cdot \frac{p_2 - p_{atm}}{R \cdot T_2}, \quad (3-7)$$

with the individual pressures p_i , starting at the pressure inside of the enclosure, which is equal to the average pressure at the regolith' surface, p_0 , and the individual temperatures T_i . The last two equations can be rewritten as

$$p_1 = p_2 + \frac{\dot{n}_1 R T_1}{c_{mol,1}}, \quad (3-8)$$

$$p_2 = p_{atm} + \frac{\dot{n}_2 R T_2}{c_{mol,2}}. \quad (3-9)$$

For this study a quasi-stationary approach to this set of equations was chosen. This results in $T_i = T_0$, $\bar{v}_i = \bar{v}_0$, and, thus, $\dot{n}_i = \dot{n}_0$. This allows to connect the equations:

$$\dot{n}_0 = \left(\frac{c_{mol,0} c_{mol,1} c_{mol,2}}{c_{mol,0} c_{mol,1} + c_{mol,0} c_{mol,2} + c_{mol,1} c_{mol,2}} \right) \cdot \frac{p_0 - p_{atm}}{R \cdot T_0}. \quad (3-10)$$

The factor $\left(\frac{c_{mol,1} c_{mol,2} c_{mol,3}}{c_{mol,1} c_{mol,2} + c_{mol,1} c_{mol,3} + c_{mol,2} c_{mol,3}} \right)$ can be seen as a correction factor to account for the resistance the gas experiences on its way through the mass spectrometer. It also results from the parallel resistances approach $\left(\frac{1}{c_{mol,0}} + \frac{1}{c_{mol,1}} + \frac{1}{c_{mol,2}} \right)^{-1}$.



Fig. 3-3: Sketch of the initial conditions study model.

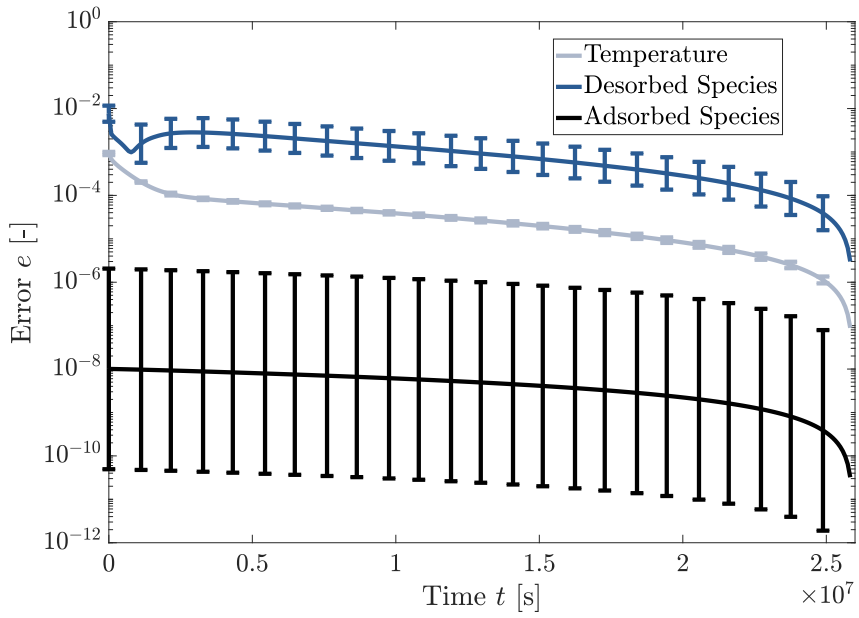


Fig. 3–4: Relative error over the simulation time of the initial conditions study for the three dependent variables, temperature, desorbed water, and adsorbed water.

3.4 Initial Conditions

In order to have a stable setup for a transient study, the initial conditions for all variables have to be set correctly, i.e. according to the underlying physics and its boundary conditions. In the initial conditions study the values for the temperature and the desorbed and adsorbed concentration of water in the lunar regolith were determined.

While the general setup with the LVS inserted in the regolith is realized as a two dimensional axisymmetric model, an undisturbed patch of lunar regolith can be modelled as a one dimensional problem. The only factor that correlates to a spatial dimension is the bulk density, which depends on the depth. Thus, all subsequent variables that depend on the bulk density, e.g. the thermal conductivity k or the porosity Φ , see sections 2.1 and 2.2, are also a function of the depth. With no dependencies on other spatial dimensions, the simulation model for the initial conditions study is a line element, representing the depth of the lunar regolith with the spatial variable z . Figure 3–3 shows the line element with a total length of 0.2 m, which is sufficiently deep to model the regolith for well over the maximum insertion depth possible by the LVS.

Furthermore, the boundary conditions at the top and the bottom end of the model are included in the figure. At the bottom of the regolith a heat flow with $q_{internal} = 0.018 \text{ W m}^{-2}$ is introduced to the domain, which corresponds to the internal heat flow of the Moon, see section 3.1. The top end of the model, which is the surface of the lunar regolith, is equipped with two DBCs, one for the temperature at the surface and one for the pressure. While the surface temperature T_{surf} is one of the parameters of the initial conditions study, the pressure is fixed to be the atmospheric pressure on the Moon of $p_{atm} = 0.3 \text{ nPa}$, which directly translates into the concentration of the desorbed species using the ideal gas law [11].

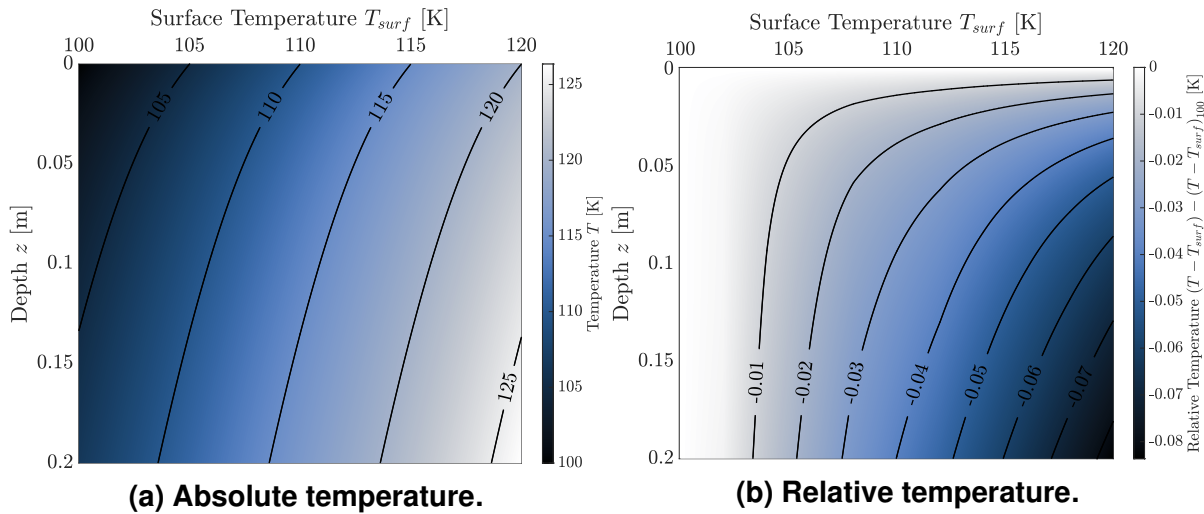


Fig. 3–5: Interpolated temperature distribution for varying surface temperatures at a water ratio of 10.0wt.%. (a): absolute, T , (b): relative, $(T - T_{surf}) - (T - T_{surf})_{100}$ compared to the temperature difference at a surface temperature of 100 K.

Since the rate of desorption, see Eq. (2–3), is nonzero even at low temperatures, no viable stationary solution can be computed. Thus, a transient simulation with a total simulation time of 300 d, or $t_\infty \approx 2.6 \times 10^7$ s, was performed. The convergence is illustrated as an error graph in Fig. 3–4. The relative error was calculated according to

$$e_T(t) = \frac{1}{N_p} \cdot \sqrt{\sum_{i=1}^{N_p} \left(\frac{T^i(t) - T^i(t_\infty)}{T^i(t_\infty)} \right)^2}, \quad (3-11)$$

$$e_d(t) = \frac{1}{N_p} \cdot \sqrt{\sum_{i=1}^{N_p} \left(\frac{c_d^i(t) - c_d^i(t_\infty)}{c_d^i(t_\infty)} \right)^2}, \quad (3-12)$$

$$e_a(t) = \frac{1}{N_p} \cdot \sqrt{\sum_{i=1}^{N_p} \left(\frac{c_a^i(t) - c_a^i(t_\infty)}{c_a^i(t_\infty)} \right)^2} \quad (3-13)$$

for each of the three dependent variables, with the total number of points of the model N_p and $(\bullet)^i$ indicating the respective value at the i -th point, and the last simulated time t_∞ . In order to get only one value for each timestep of the simulation, the sum of all relative errors at each point is calculated.

Figure 3–4 shows the relative error for the three dependent variables, the temperature, the desorbed and adsorbed species. The convergence goes down to an error of as little as 1×10^{-13} for the adsorbed species and, thus, has the least relative error of the three dependent variables. For the temperature a final value of about 1×10^{-7} , and for the desorbed water a final value of 1×10^{-6} is reached.

The three Figs. 3–5 to 3–7 show the results of the initial conditions study for the three main dependent variables T , c_d , and c_a of the simulation. For each of the variables the results are shown in an absolute and a relative manner. The former illustrates what

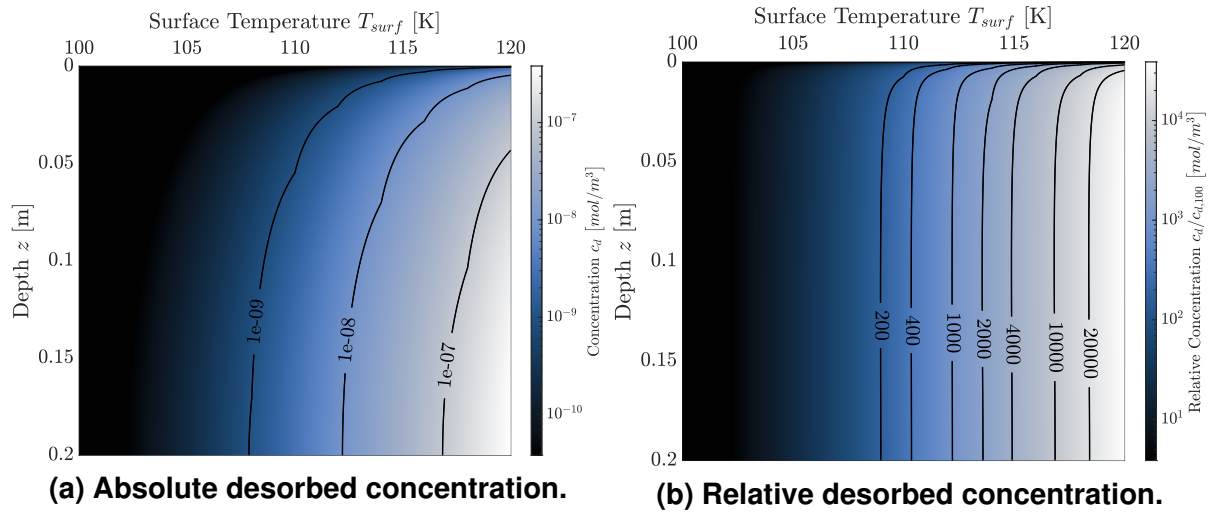


Fig. 3–6: Interpolated concentrations of the desorbed water at a total water ratio of 10.0 wt.%. (a): absolute, c_d , (b): relative, $c_d/c_{d,100}$ compared to the solution at a surface temperature of 100 K.

the actual values used as initial conditions are, while the latter better demonstrates the differences between the solutions and their order of magnitude.

Temperature Figure 3–5 shows the initial conditions for the temperature with respect to the surface temperature T_{surf} , the depth z , and the water ratio. Both subfigures illustrate the results for a water ratio of 1.0 wt.% where the other two parameters are interpolated to create the colormap.

As expected, the temperature at $z = 0.0$ m equals the surface temperature T_{surf} . With increasing depth the temperatures also rise. At 20 cm the temperature is already about 5 K higher compared to the surface. This increase comes from the internal heat flow of the Moon, which is introduced at the bottom of the model. The shape of the temperature distribution is governed by the thermal conductivity k . As shown in Sec. 2, the thermal conductivity is a function of the temperature, the pressure, and the depth of the regolith. Generally, higher temperatures lead to higher pressures and both variables lead to higher thermal conductivities, see Fig. 2–3. Thus, the regolith should be better at conducting the heat at higher T_{surf} . This exact behavior can be seen in Fig. 3–5b, where the temperature increase relative to the one at $T_{surf} = 100$ K is plotted. At a surface temperature of 120 K the regolith experiences a smaller temperature increase of nearly 0.1 K at 20 cm depth.

Desorbed Water Figure 3–6 shows the results for the desorbed water, as before as a function of the surface temperature, the depth, and the water ratio. Unlike before, most of the colormap shows no change at all, which is due to the fact that the desorption process is mainly driven by the frequency factor k_d . This factor is going exponentially with the temperature and, thus, needs to exceed a certain temperature until desorption takes place in a reasonable amount of time¹. It can be seen that only at tempera-

¹ $t \approx 10^8$ s

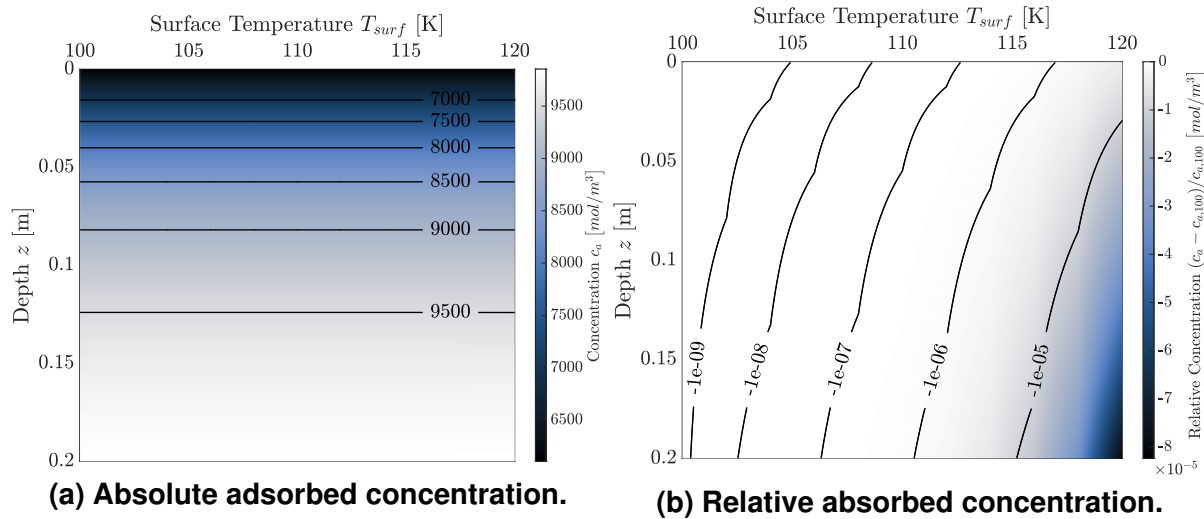


Fig. 3–7: Interpolated concentrations of the adsorbed water at a total water ratio of 10.0wt.%. (a): absolute, c_a , (b): relative, $(c_a - c_{a,100})/c_{a,100}$ compared to the solution at a surface temperature of 100 K.

tures of more than 120 K some desorbed water occurs. The right side of the figure shows the relative difference of the desorbed concentration compared to the one at a surface temperature at 100 K which hints at the order of magnitude of c_d . Since the scale goes up to 1×10^4 , the desorbed concentration at 120 K is four orders of magnitude higher compared to lower surface temperatures, which, thus, are at approximately $1 \times 10^{12} \text{ mol m}^{-3}$, which is close to what the atmospheric pressure would induce as a desorbed species.

Adsorbed Water The last figure, Fig. 3–7, shows the absolute and the relative initial values of the adsorbed water concentration which, as before, depend on the surface temperature, the depth, and the water ratio. Likewise, the shown graphs depict the results for a water ratio of 1.0 wt.%. The absolute results, shown on the left, illustrate that the results are very uniform across all surface temperatures. The only gradient visible is the one in the direction of the depth, which directly correlates with the setup and handling of the water ratio. For the simulation, the water concentration is introduced to every point equally, at a certain percentage of the regolith's weight. Since the density of the regolith increases with the depth, the respective mass of each point increases with a higher z . Thus, the absolute concentration of the adsorbed water also increases with the density of the regolith.

The graph on the right depicts the relative difference of the adsorbed species as $(c_a - c_{a,100})/c_{a,100}$. Compared to the previous figure of the desorbed species, see Fig. 3–6, the loss of water as adsorbed concentration mirrors the gain of water as the desorbed concentration. Only at high enough temperatures desorption occurs, which, as shown in both figures, does not happen under about 120 K.

To summarize, the initial conditions were calculated using a one dimensional transient simulation modelling the change over a total period of 300 d, which resulted in lookups

tables for the three dependent variables shown in Figs. 3–5 3–6 and 3–7. Those values were used to interpolate the respective initial conditions for the 2D-axisymmetric simulation based on the given surface temperature and the expected water ratio bound inside of the soil.

3.5 Model and Solver Setup

The following section presents multiple studies used to evaluate the quality of the results based on certain model and solver settings. Here, the mesh size, the domain size, and the maximum timestep of the solver are discussed.

3.5.1 Mesh Study

In order to verify the simulation, several preliminary studies were performed. The first one of those studies was the mesh study which took a closer look at the quality of the results as a function of the mesh or, more precisely, the size of the mesh elements and subsequently the number of mesh elements.

The mesh generally consists of two main areas, the enclosure of the LVS including its drillshell and heating rod as well as the regolith and gas in between, and the surrounding regolith. The former is spatially discretized using a structured grid mesh while the latter is build using a free triangular mesh.

In order to parametrize the mesh, a total of two COMSOL Multiphysics specific parameters were used; h_{max} , a measure of the maximum size of a single mesh element, and h_{grad} , a measure of the maximum growth rate of two adjacent mesh elements. The former governs the size of the structured mesh, as all elements take on an edge length equal to h_{max} . The latter then defines the triangular mesh, specifically how the elements grow in the direction of the outside boundaries of the regolith starting from a size of h_{max} at the enclosure.

The mesh study analyzes the effects of the variation of these two parameters. In order to measure the effect, the mean squared error, according to

$$\bar{e}_T = \frac{1}{N_t N_p} \sum_{i=1}^{N_t} \sum_{j=1}^{N_p} \left(\frac{T^j(t_i) - T_{ref}^j(t_i)}{T_{ref}^j(t_i)} \right)^2, \quad (3-14)$$

$$\bar{e}_d = \frac{1}{N_t N_p} \sum_{i=1}^{N_t} \sum_{j=1}^{N_p} \left(\frac{c_d^j(t_i) - c_{d,ref}^j(t_i)}{c_{d,ref}^j(t_i)} \right)^2, \quad (3-15)$$

with the total number of evaluated timesteps N_t , the total number of compared data points N_p , the i-th timestep t_i , the j-th data point of the respective variable $(\bullet)^j$, and the reference value $(\bullet)_{ref}$. The finest mesh taken for the reference values was calculated for every combination of the parameters h_{max} and h_{grad} .

The results are shown in Fig. 3–8. The total of 18 simulations are forming two clearly separate groups, which can be distinguished by the respective h_{max} value of the simulation. While inside of the groups the resulting errors only vary very little, as indicated by the zoomed in section of Fig. 3–8, changing h_{max} to 5×10^{-4} m significantly improves the results by a factor of roughly 1.3 for both the desorbed species and the

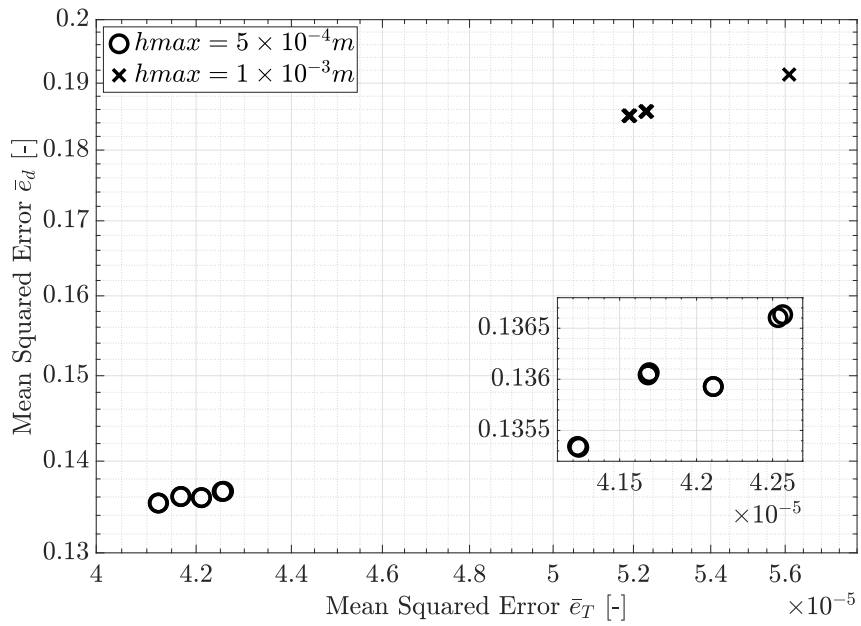


Fig. 3–8: Mean squared errors of the mesh study.

temperature. Thus, the second parameter, $hgrad$, does not play a significant role in the results and was set to its upper boundary to decrease the total number of elements in the simulation and, thus, reduce the computational effort.

3.5.2 Domain Study

Another study to verify quality of the simulation results was the domain study which took a closer look at the size of the regolith domain. Since the water vapor pressure spreads through the entire regolith surrounding the LVS, having impenetrable boundaries encasing the gas can influence the results. Similar to the mesh study, two parameters were varied, the diameter d and the height h of the cylindrical regolith domain.

The comparison was handled analogous to the mesh study with the mean squared errors calculated according to Eqs. (3–14, 3–15). In this case the chosen reference simulation was the one simulation with the biggest regolith domain. As before, the results of the 20 simulations appear as groups in Fig. 3–9, which shows the means squared error for both the temperature and the desorbed volatile water. These groups can be distinguished by the respective diameter d of the simulation, with an increasing diameter leading to smaller errors. While those simulations with a diameter of ≥ 1.5 m already merge and show only minor differences, $d = 1.0$ m leads to slightly higher errors, and $d = 0.5$ m to errors about 1.2 to 2 times as high. Inside of the groups a dependence on the height of the soil is visible though less significant compared to the influence of the domain's diameter. In order to reduce the computational effort and still reach low errors for the dependent variables, a diameter of $d = 1.0$ m and height $h = 1.0$ m was chosen, which corresponds to the simulation with the lowest errors out of the group of $d = 1.0$ m.

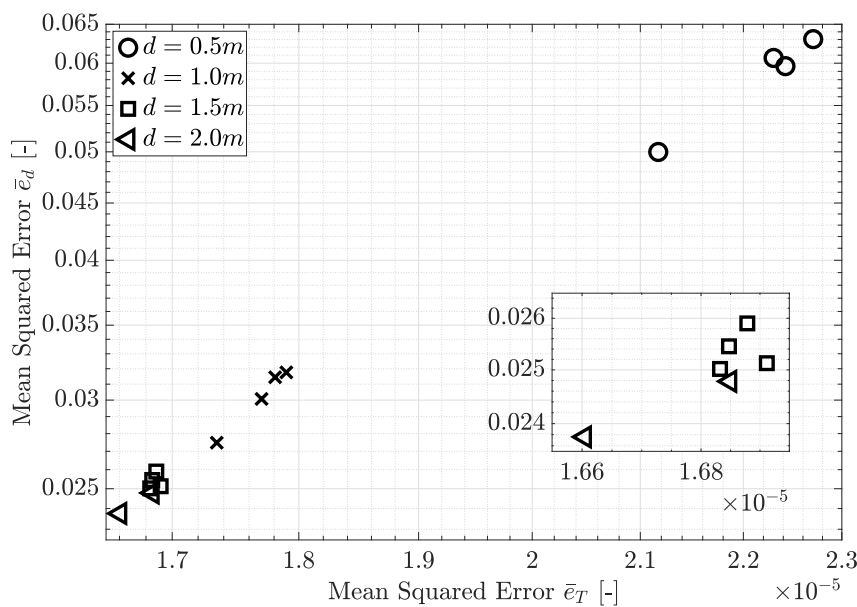


Fig. 3–9: Mean squared errors of the domain study.

3.5.3 Timestep Study

In order to show the stability of the solver, a timestep study was performed. Here, the maximum timestep the COMSOL Multiphysics solver was allowed to take was varied. Generally, the solver always chooses the next timestep based on the convergence and the residual of the computation of the previous timestep. If these two values were better than a certain internal threshold, the solver doubles the timestep for the next computation. Should the desired output time specified by the user not fall on the time chosen by the solver, which is generally the case, then the output is calculated through interpolation. Since this interpolation could potentially hide some effects of the dynamic system from the output, limiting the maximum timestep size is a commonly used technique.

The solver internally places a limit of one-tenth of the maximum simulation time for the timestep, which leads to $\Delta t_{max} = 360$ s for an one hour simulation. This setting is marked as *free* in the following. Figure 3–10 shows the mean squared error for the temperature and the desorbed water concentration for varying maximum timesteps. As before, the values were calculated using Eqs. (3–14, 3–15), this time using the simulation with the smallest maximum timestep of $\Delta t_{max} = 10$ s as the reference case. As expected, the errors increase with an increasing timestep for both dependent variables, especially for the desorbed species the effect spans multiple orders of magnitude.

While the obvious choice for the optimal timestep value seems to be the smallest possible one, it comes with severe setbacks concerning the computational effort. Already cutting the maximum timestep size in half roughly doubles the number of evaluated times during the simulation, leading to approximately twice the simulation time². Thus, reducing the timestep by a factor of $\frac{1}{36}$ turned the initial 30 min simulation to one running multiple days.

²This approximation is only valid for simulations with continually increasing timesteps until reaching the maximum. In reality, the effect is slightly less drastic.

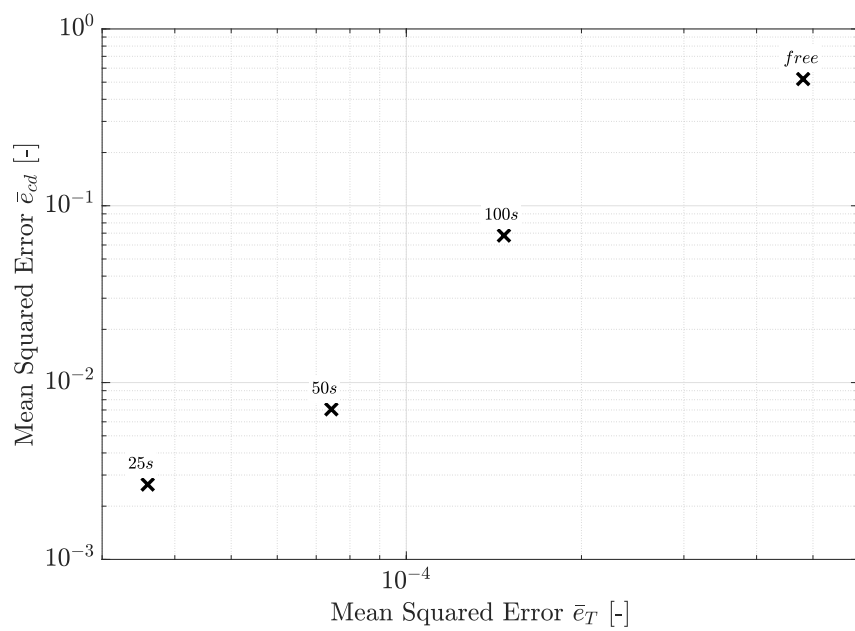


Fig. 3–10: Mean squared errors of the timestep study.

Accounting for both effects, a final value of $\Delta t_{max} = 50$ s was chosen for the solver.

4 Results

This chapter presents the results of the simulation study with respect to each individual variable. First, the results of the baseline simulation are shown. Second, the influence of the water ratio Ψ , is analyzed. Third, the results of varying the desorption energy E_d are presented. Last, additional variations that have been performed are discussed including the gas permeability and the solid conductance factors.

In order to be able to properly compare the results of the different studies with one another, a fixed combination of the parameters has been chosen as a baseline setup. Said parameter values can be seen in Tab. 4–1. Based on these parameters, every subsequent study analyzed the effects of varying one single parameter while keeping all the others at their baseline-state.

4.1 Baseline

The baseline simulation is a result of the baseline parameters listed in Tab. 4–1 without any further variation of any parameters. Figure 4–1 shows for each dependent variable the resulting field at the end of the simulation.

The temperature distribution, shown on the left of the figure, reaches from about 200 K to nearly 1350 K close to the heating rod. Due to the low thermal conductivity of the regolith, see Sec. 2.2, the heating of the soil was not able to reach areas further than approximately 5 cm away from the source, which results in steep gradients and high peak temperatures. An additional factor slowing down the spread of the temperature is the geometric nature of the 2D-axisymmetric model. Since the volume increases quadratically with an increasing r-coordinate, it takes even more energy to heat up regolith layers further out from the center at $r = 0$ m.

On the far right the adsorbed water distribution is shown, which features a sharp edge around the LVS at which the adsorbed species completely decreases from its initial value of around 200 mol m⁻³ to zero. When compared with the temperature distribution, one can see that the area of zero adsorbed water has a similar shape to that of the

Tab. 4–1: Parameters of the baseline setup.

Symbol	Value	Description
Ψ	0.25 wt.%	water ratio
E_d	0.6 eV	desorption energy
$k_{g,a}$	$6 \times 10^{-12} \text{ m}^2$	gas permeability
C_1	0.5	factor of solid conductance k_s , Eq. (2–22)
C_2	0.38	factor of solid conductance k_s , Eq. (2–22)

Tab. 4–2: Most important numerical solver settings.

Parameter	Value
Time Stepping Method	BDF
Initial step	0.001 s
Maximum step	50 s
Solver type, heat transfer	direct
Solver type, mass transfer	iterative

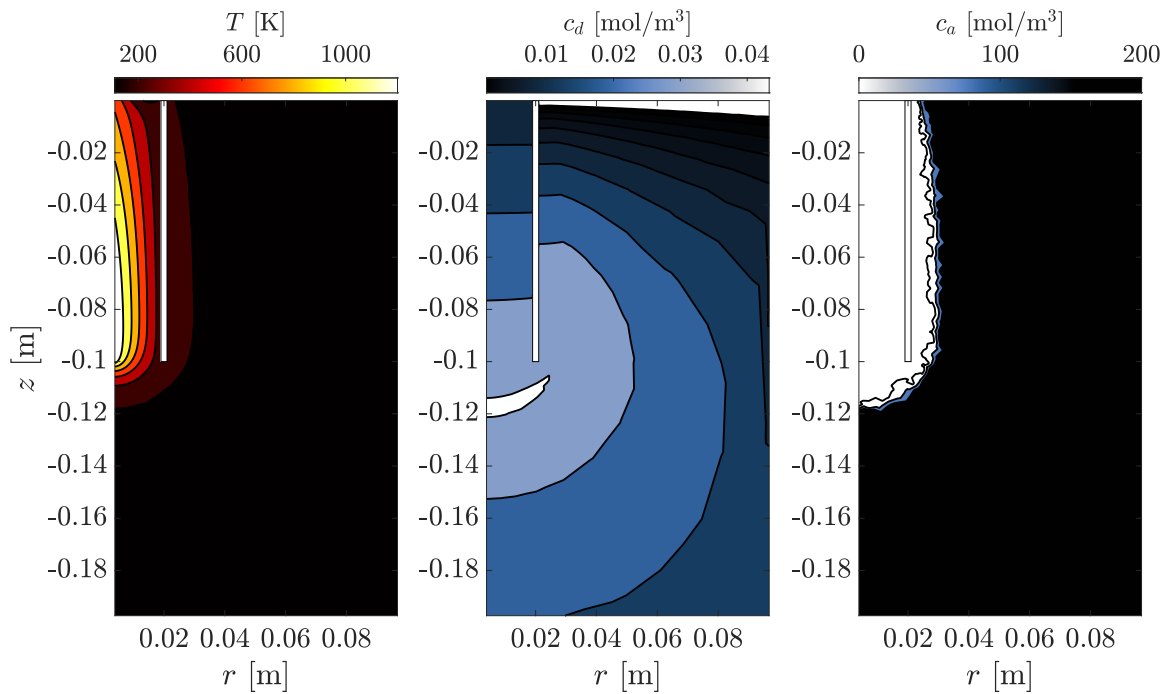


Fig. 4–1: Results of the baseline simulation.

temperature. This behavior clearly originates from the temperature dependent rate constant which is the driving factor of the desorption. For a given desorption energy the threshold temperature at which some meaningful desorption starts happening can be found by solving

$$k_d = 1 \frac{1}{\text{s}} = \frac{k_B \cdot T}{h} \cdot \exp\left(\frac{-E_d}{k_B \cdot T}\right) \quad (4-1)$$

which, according to Eq. (3–2), states that the entire remaining c_a would desorb in 1 s. Iteratively solving for the temperature at baseline conditions results in the threshold temperature of 238.1716 K. The area of the temperature distribution with T of at least 238.1716 K matches very closely the area of fully desorbed water, proving that the temperature dependent rate constant k_d dictates the size and shape of the adsorbed water distribution.

The desorbed water presented in the middle of Fig. 4–1 ranges from about 0 mol m⁻³ to little over 0.4 mol m⁻³ with its peak located right under the LVS. From this position the

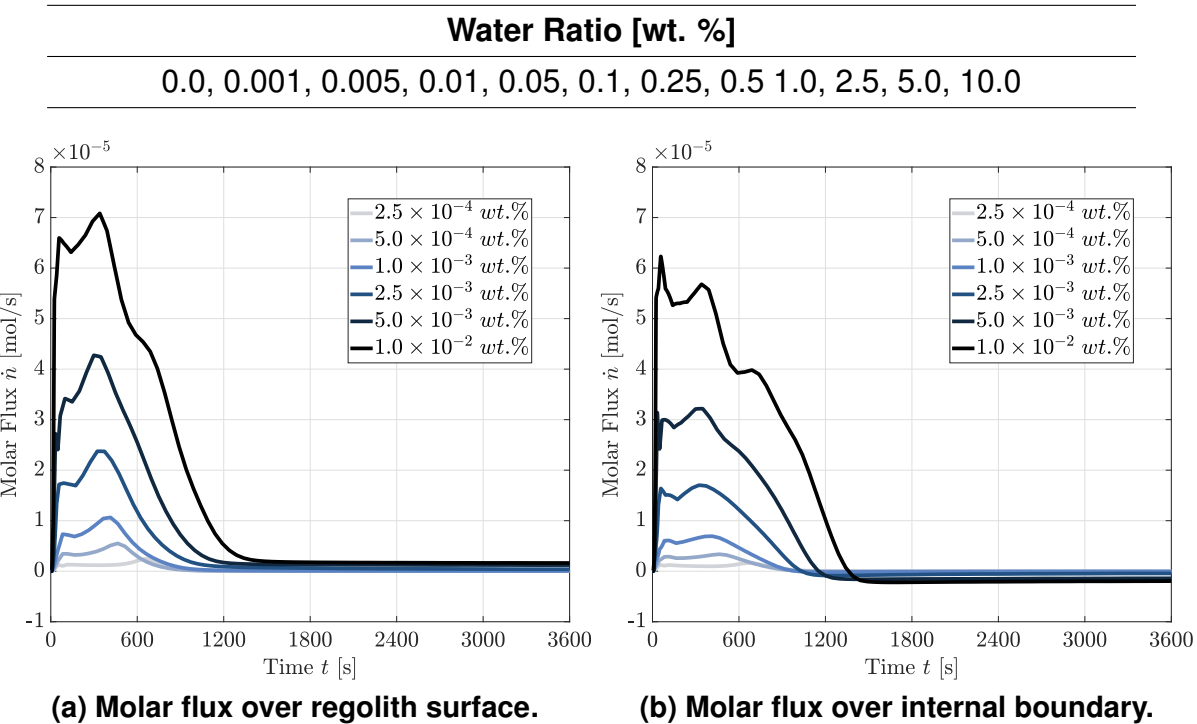
Tab. 4–3: Values for the water ratio study.

Fig. 4–2: Molar flux over (a) the regolith surface inside of the LVS' enclosure and (b) over the internal boundary of the regolith domain leading inside of the LVS' enclosure for varying water ratios Ψ .

values decrease radially outwards. The location of the peak desorbed species overlaps with the lower edge of the fully desorbed area, shown in the right part of the figure. This indicates that right at this lower edge the most water gets desorbed, dominating every other mass transfer mechanism at the end of the 3600 s long simulation. This effect is further strengthened by the geometric nature already explained for the temperature distribution. With the desorption being very closely related to the increasing patch of the threshold temperature at which meaningful desorption can happen and the temperature spread being slowed down radially due to the 2D-axisymmetry, it makes sense that the area of maximum desorption is located underneath the instrument where the temperature spread at the end of the simulation should be the fastest.

While Fig. 4–1 shows a 2D patch of the results surrounding the center of the LVS, the subsequent studies will focus more on the behavior and distributions inside of the regolith in the enclosure. Since the adsorbed species tends to be completely zero for the entire patch inside of the enclosure at some point of the simulation, the focus was set on the temperature and the pressure distributions. The latter can be calculated using the ideal gas law and is, thus, a combination of both the temperature and the desorbed species.

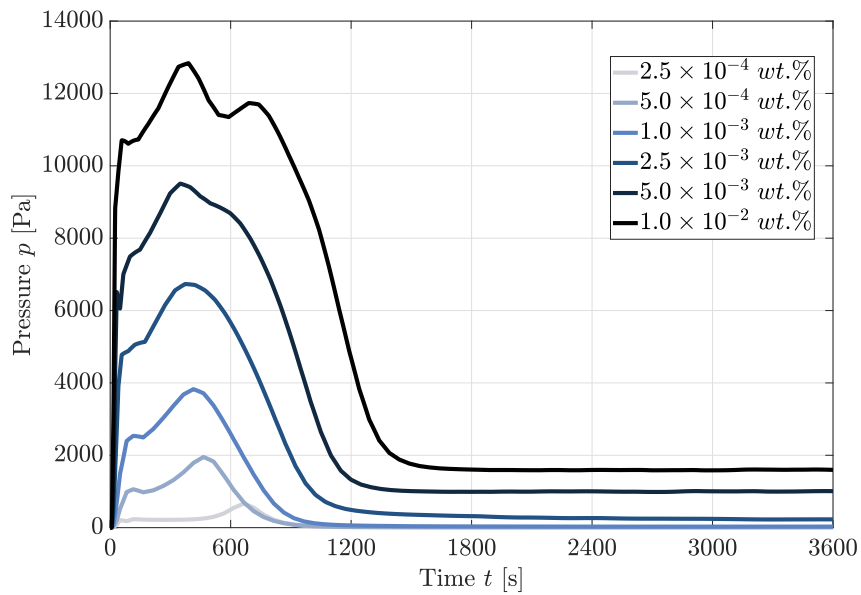


Fig. 4–3: Average water vapor pressure of the regolith domain inside of the LVS’ enclosure for varying water ratios Ψ .

4.2 Water Ratio Study

For the study of the influence of the water ratio Ψ on the simulation, a set of values have been simulated. The values can be found in Tab. 4–3. Figure 4–2 shows the result for the molar flux for different values of Ψ . On the left side the flux over the regolith surface inside of the LVS’ enclosure is shown, while the left side presents the flux over the internal regolith boundary leading upwards into the LVS’ enclosure, see Fig. 1–1.

As expected, the mass transport increases with a higher water ratio, since more water can be desorbed and, thus, move through and out of the soil. In both graphs all the simulations show two peaks, one immediately after the beginning of the simulation and one after approximately 8 min. The first peak is a result of the initial conditions of the LVS drill, which is set to 200 K in order to model that the main body of the instrument is not allowed to reach temperatures below a certain threshold, preventing sensitive equipment from being damaged. Thus, the soil close to any part of the instrument is quickly reducing the temperature gradient by absorbing the heat from the drill. Since this rapid heat exchange is already enough for the regolith to reach temperatures high enough for volatile desorption, the first peak occurs almost immediately.

The second peak is the result of the thermal extraction by powering the heating rod. With increasing simulation time more and more of the regolith reaches temperatures leading to a high enough desorption rate k_d for meaningful desorption to take place. Once all of the adsorbed water’s bond have been broken additional volatiles can only come from the mass transport mechanisms through the regolith. Thus, the mass loss through the molar flux depicted in Fig. 4–2a can only be compensated through the molar flux shown in Fig. 4–2b. Since due to the low thermal conductivity the temperature cannot spread quick enough downwards to keep desorbing water to be transported in the LVS’ enclosure, the molar fluxes continually decrease after the second peak. After

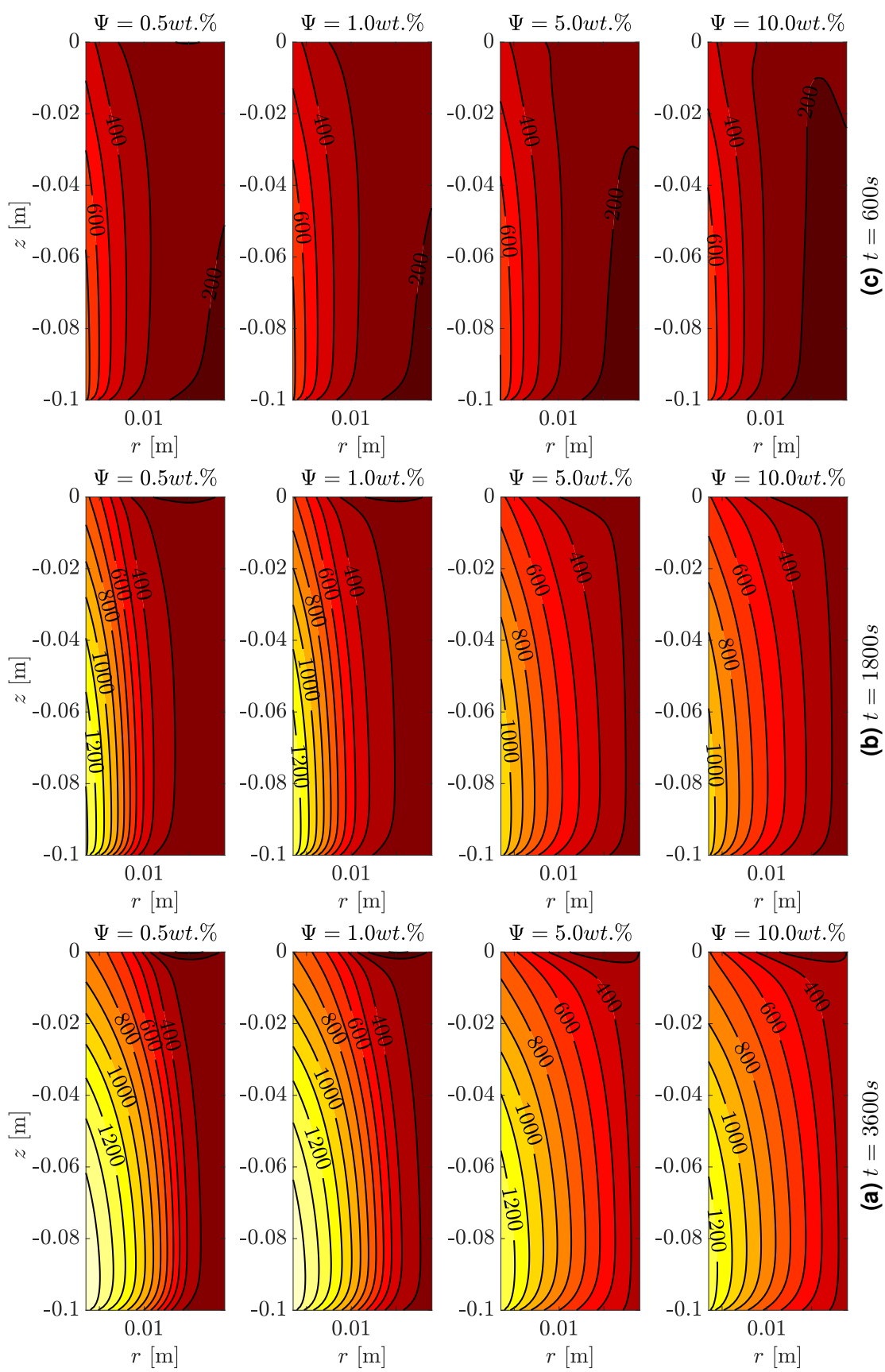


Fig. 4-4: Temperature distribution T in [K] of the regolith inside of the LVS' enclosure for varying water ratios Ψ at three different times of the simulation.

Tab. 4–4: Values for the desorption energy study.

Desorption Energy [eV]
0.4, 0.6, 0.8, 1.0, 1.2, 1.4, 1.6, 1.8, 2.0

roughly 20 min the molar flux over the regolith surface stagnates at a value little over 0 mol s^{-1} . It does not reduce to zero due to the little vapor pressure left in the regolith, creating a pressure gradient $p - p_{atm}$ needed for the mass flux through the orifices, see Sec. 3.3.

The average pressure is shown in Fig. 4–3. Due to the connection of the pressure and the molar flux presented in Eq. (3–10), the shape of the average pressure is directly connected to the shape of the flux depicted in Fig. 4–2a. As before, the pressure increases with higher water ratios with the two peaks being visible. It also stagnates after approximately 20 min, leading to a nearly constant average pressure for the remaining two-thirds of the simulation.

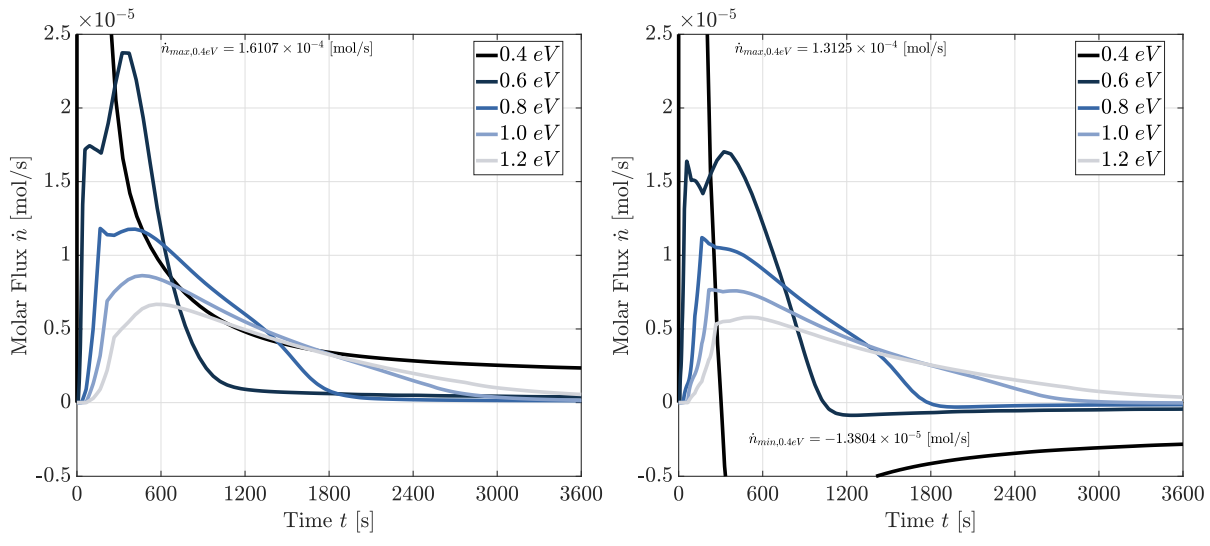
Lastly, Fig. 4–4 shows the temperature distribution of the regolith inside of the enclosure for varying water ratios at three different times of the simulation. All the previously explained effects can be seen in the evolution of the temperature through the soil. While the temperature close to the heating rod is reaching the highest values, near the drill shell it is nearly constant during the entire simulation, leading to steeper gradients with increasing physical time.

The effects of the water ratio on the temperature distribution are linked to the pressure inside of the lunar soil, which increases with higher Ψ . The pressure leads to a significantly improved thermal conductivity, see 2–3, with smoothens the temperature gradient, spreading the temperature more evenly and essentially reducing the peak temperature. Especially in Fig. 4–4a, which shows the distribution at the end of the simulation, this effect can be clearly observed as the study with $\Psi = 10.0\text{wt.\%}$ just barely reaches the 1200 K as its maximum temperature.

4.3 Desorption Energy Study

The second main parameter that was analyzed is the desorption energy E_d as a measure of the strength of the bond between the volatile water and the regolith particle. Thermal extraction introduces energy into the soil until enough energy is present to break the bond and desorb the volatile. Thus, a higher desorption energy means that only at higher temperatures meaningful desorption will take place. This is directly connected through the rate constant k_d , see Eq. (2–3).

Table 4–4 show the values of the desorption energy analyzed during the study. While explained in Sec. 2.1, the desorption energy depends on the kind of bond between the volatiles and its respective particle, which has been analyzed to be approximately 0.45 eV to 1.2 eV for lunar regolith and its simulants, this study also looked at some values outside of that range. This allowed to capture a general trend coming from the variation of the desorption energy, which is discussed in the following.



(a) Molar flux over regolith surface.

(b) Molar flux over internal boundary.

Fig. 4–5: Molar flux over (a) the regolith surface inside of the LVS' enclosure and (b) over the internal boundary of the regolith domain leading inside of the LVS' enclosure for varying desorption energies E_d .

Figure 4–5 shows the molar flux over the the surface of the regolith inside of the LVS' enclosure and over an internal boundary of the regolith leading into the enclosure, respectively. The graphs were cropped to better capture the behavior of the molar flux with increasing desorption energy. Maximum and minimum values not shown on the plot are given on the figure. As expected, the flux is greatly influenced by the desorption energy with increasing E_d leading to lower fluxes and later peak values. While the results on Fig. 4–5a are purely positive due to the definition of the molar flux over the surface, see Eq. (3–10), the fluxes on Fig. 4–5b also reach negative values.

This behavior results from the delayed desorption happening due to higher energies necessary for breaking the bond between the volatile and the particle. With higher E_d the rate constant k_d is generally lower compared to other simulations at the same physical time. This leads to fewer desorbed volatiles and, thus, a lower pressure, as seen in Fig. 4–6. Additionally, the moment of peak pressure occurs later along the simulation since higher temperatures need to be reached to desorb volatiles from the regolith. The resulting effects on the temperature distribution can be seen in Fig. 4–7. It shows the distribution at three different times during the simulation and for four different desorption energies. Generally, higher temperatures occur for higher E_d and, thus, for lower pressure. As it was with the water ratio study, the increased pressure leads to an increased thermal conduction k , which then leads to a more evenly distributed temperature field.

4.4 Additional Studies

This section covers the results of the variation of the gas permeability and the factors C_1 and C_2 of the solid thermal conductance k_s , see Eq. (2–22).

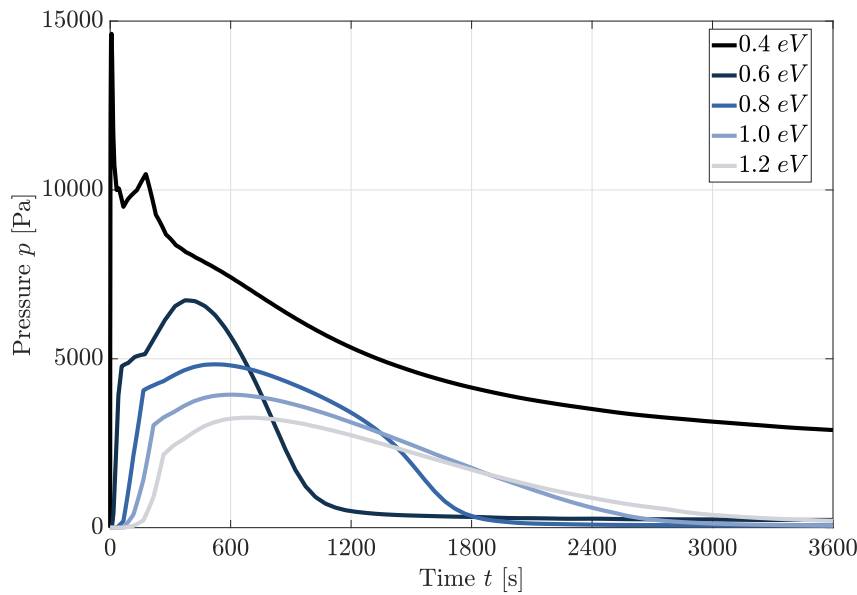


Fig. 4–6: Average water vapor pressure of the regolith domain inside of the LVS' enclosure for varying desorption ratios E_d .

4.4.1 Gas Permeability

While changes in the molar flux due to any change in the gas permeability of the regolith are negligible, the average pressure inside of the regolith domain in the LVS' enclosure changes due to a changed convection coefficient of the mass transfer. Figure 4–8 shows the results for four different gas permeabilities inside of the plausible range for lunar regolith [7]. As expected, the average pressure decreases with better permeability and, thus, more convective mass transfer, smoothing the pressure distribution. As before, the pressure inside of the regolith changes the thermal conductivity of the soil, which in turn has an effect on the temperature distribution. Figure 4–9 shows the difference of the temperature distribution inside of the regolith of the LVS' enclosure between the two simulations with a gas permeability of $1 \times 10^{-12} \text{ m}^2$ and $7 \times 10^{-12} \text{ m}^2$ at the end of the simulation time. This format was chosen to better illustrate the changes in the temperature distribution. Unlike before, the maximum absolute difference is only about 10 K with the maximum occurring close to the heating rod, where the highest temperatures and according to the ideal gas law also the highest pressures are expected. There, a higher permeability leads to the highest difference of the mass transport due to convection and, thus, also to the highest differences in pressure and temperature across the different simulations.

4.4.2 Solid Thermal Conductance

The factors of the solid thermal conductance influence the behavior of the temperature distribution in the soil. For this study, the six different materials listed in Tab. 2–3 with the according factors C_1 and C_2 were analyzed. A comparison and closer analysis can be found in the appendix, App. A.

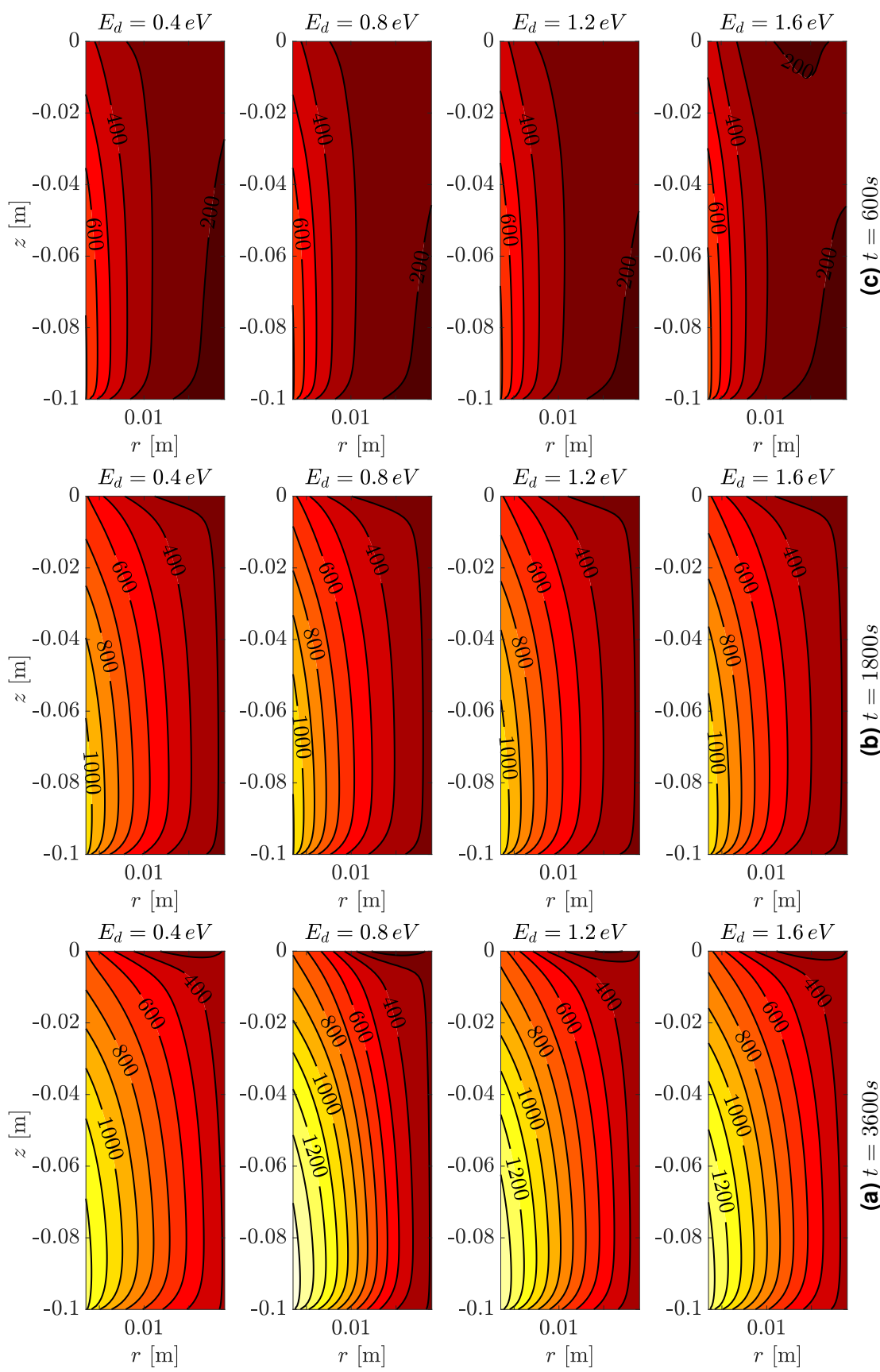


Fig. 4-7: Temperature distribution of the regolith inside of the LVS' enclosure for varying desorption energies E_d at three different times of the simulation.

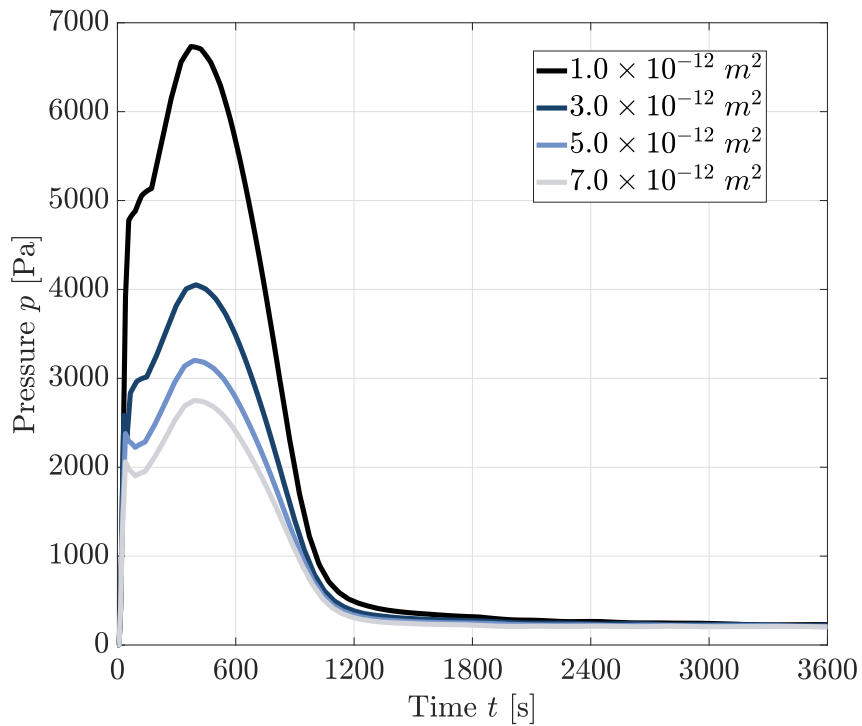


Fig. 4–8: Average pressure inside of the regolith of the LVS' enclosure.

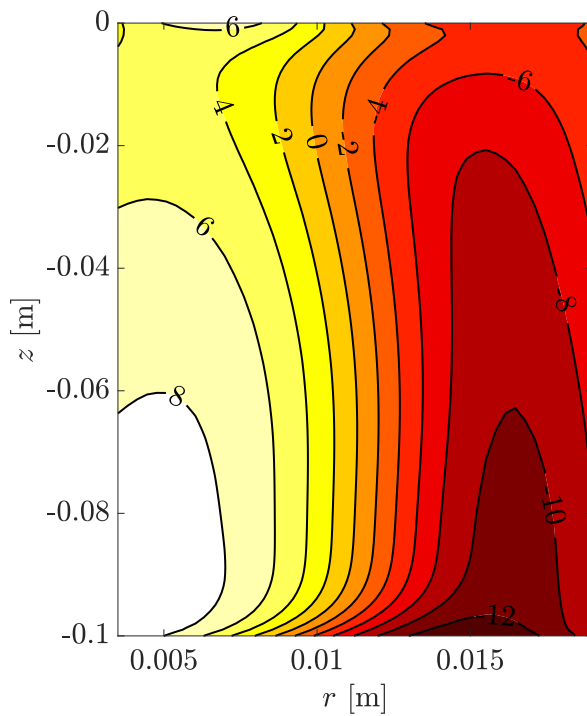


Fig. 4–9: Temperature difference distribution ΔT [K] between $k_{Ba} = 1 \times 10^{-12} \text{ m}^2$ and $7 \times 10^{-12} \text{ m}^2$ at the end of the simulation time.

5 Correlation Study

The following chapter covers an overview on the correlation study including the experimental setup, the needed adjustments for the simulation model as well as the results of the study.

The environment of the lunar surface had to be simulated for the thermal extraction tests of the LVS. For this, a vacuum in a dynamic thermal environment had to be created, handled by a vacuum chamber. While the present vacuum chamber could only reach 2×10^{-5} mbar, which is significantly higher than the atmospheric pressure on the lunar surface, it generally offers a difference of several magnitudes compared to the pressure inside of the LVS' enclosure [25].

In order to copy the expected situation during the LVS' mission, a sample containing a high volatile ratio was prepared inside of a container in which it was cooled down to -100 °C using liquid nitrogen. While this study showed the effects of the thermal environment, the experimental study focused on the general concept of thermal extraction and tested at environmental temperatures of 15 °C to 25 °C [25].

The sample consisted of JSC-1A lunar regolith simulant inside of a 10×10^{-3} m³ stainless steel bucket. The choice of the simulant provided a similar particle size compared to the expected regolith, as well as similar bulk densities of around 1.6 g cm⁻³ to 1.6 g cm⁻³ for dry samples. To moisturize the sample a specific amount of water was added prior to the experiment. The sample was mixed to create an even water distribution without clumps.

After an initial functionality test the operational test was performed which included a bakeout after the evacuation, the drilling into the sample, followed by a 90 min heating through powering the heating rod. At the end of the test the drill is retracted.

In order to accurately simulate the experimental setup, some of the boundary and initial conditions had to be adjusted. When compared with Fig. 3–2, the internal heat at the bottom of the sample was not included and the pressure boundary at the surface of the regolith was set to the ambient pressure inside of the vacuum chamber. Additionally, the \dot{n}_0 molar flux of the sample's surface inside of the enclosure was adjusted, since no mass spectrometer was mounted to the instrument during the testing. This reduces the amount of chambers and orifices by one and, thus, according to Eq. (3–4) increases the molar flux.

For the initial conditions, the temperature and pressure was set to the ambient conditions of the vacuum chamber without any depth dependencies.

Figure 5–1 shows the pressure and temperature readout of one of the verification test performed for the volatile extraction instruments. While the setup of the experiment was mirrored for the simulation model, both variables are hardly matching the results

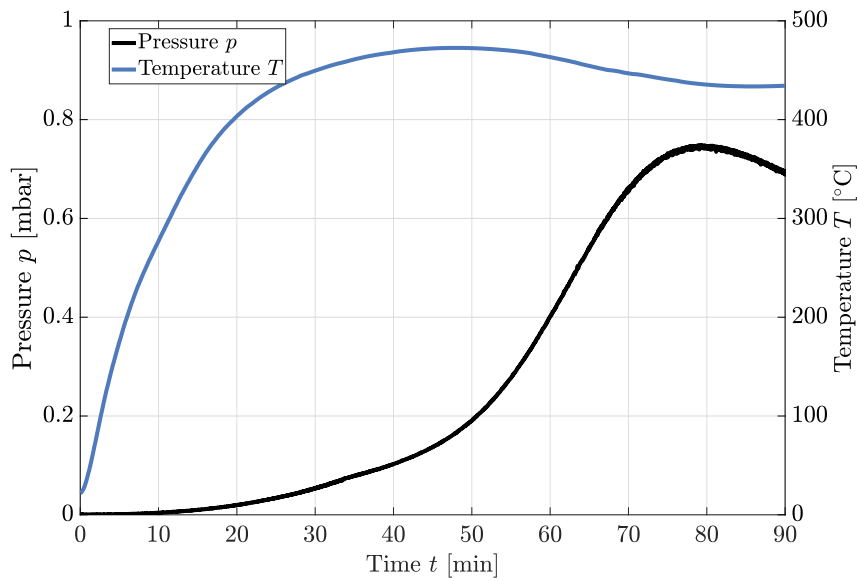


Fig. 5–1: Results of the thermal extraction verification test [25] with a sample.

coming from the simulation. Even for the most conservative choice of the desorption energy, the temperature still stays about 200 K to 300 K below the simulation results, compare Figs. 4–4 and 4–7. While the magnitude of the pressure can be adjusted using higher values for the desorption energy, the distinguished peak close to the end of the experimental data could not be reproduced.

This difference in behavior could be explained by several factors. For the temperature the lower values have to be caused by a significantly improved thermal conduction of the used regolith simulant. Additionally, an improved model of the radiative heat transfer between the surfaces of both the regolith and the LVS as well as the environment might further lower the temperatures of the simulation. For the mass transport it seems that an important effect leading to the delayed peak pressure is missing in the description of the numerical model. One explanation could be the missing resorption process of the volatiles, which would slow down the desorption and could potentially delay the moment of peak pressure inside of the enclosure. Together with an adapted description of the desorption energy of the bonds of the simulant it might play a role bigger than anticipated in the temperature range up to 400 °C.

While these factors might play a key role for a possible correlation study, one should also work on an improved description of the material properties, which heavily influence the thermal conductivity as well as the determination of the corresponding desorption energy E_d . Additionally, improving the instrumentation setup of the experiments in order to achieve more accurate results may be beneficial for a possible correlation.

6 Conclusion and Outlook

This work presented the implementation of a simulation model including the heat and mass transfer during the thermal extraction using the LVS, as well as the results of the parameter studies using the parametrized model.

First, the mathematical description of the underlying processes were presented for both the mass and the heat transfer. Secondly, the numerical model including the setup of the geometry, the boundary and initial conditions, as well as the numerical solver are shown. Afterwards, the results of the main studies are included. These are the water ratio study investigating the effects of varying water contents in the regolith domain, and the desorption energy study taking a closer look at the influence of the strength of the bond between the volatiles and the particles. Some additional studies for parameters with minor effects, like the gas permeability and solid conductance, were also presented.

The key take-aways of the results were that the method of thermally extracting the volatiles from the regolith works and produces a molar flux over the surface inside of the LVS to be measured by a mass spectrometer. Furthermore, contrary to initial belief the mass transfer mechanisms mostly transport desorbed water from outside of the LVS into its enclosure and not the other way around. Thus, future analyzes have to account for additional volatiles from underneath the instrument instead of lost volatiles escaping through the opening.

An experiment concerning the thermal extraction of volatiles was presented including the adjustments of the simulation model for a correlation study. Even though a close correlation between the measured and the simulated results was not possible with the current model, an explanation of the different effects as well as suggestions for further analyzes were presented.

Future work shall include a nondimensionalized description of the problem as well as a more elaborate description of the mass transport over the regolith surface and through the instrumentation. The latter may include modelling the thermo-fluid behavior of the gaseous phase inside the enclosure, which might include condensation at cold surfaces which could potentially have a significant influence on the thermal behavior of the LVS. Additionally, improving the mass transfer description by introducing resorption to the model might also be important. While currently resorption is believed to only have a minor effect due to the high temperatures, it could play a bigger role than anticipated, especially during the heat up process. Also, a working correlation study as well as a extensive uncertainty analysis shall be performed.

Bibliography

- [1] *COMSOL Multiphysics® v. 5.3*, COMSOL AB, Stockholm, Sweden, 2020, www.comsol.com.
- [2] *MATLAB version 9.9.0.1570001 (R2020b) Update 4*, The Mathworks, Inc., Natick, Massachusetts, 2020.
- [3] P. O. Hayne, J. L. Bandfield, M. A. Siegler, A. R. Vasavada, R. R. Ghent, J.-P. Williams, B. T. Greenhagen, O. Aharonson, C. M. Elder, P. G. Lucey, and D. A. Paige, “Global regolith thermophysical properties of the moon from the diviner lunar radiometer experiment,” vol. 122, pp. 2371–2400, 2017.
- [4] S. J. Barber, I. P. Wright, F. Abernethy, M. Anand, K. R. Dewar, M. Hodges, P. Landsberg, M. R. Leese, G. H. Morgan, A. D. Morse, J. Mortimer, H. M. Sargeant, I. Sheard, S. Sheridan, A. Verchovsky, F. Goesmann, C. Howe, T. Morse, N. Lillywhite, N. Quinn, A. Missaglia, M. Pedrali, P. Reiss, F. Rizzi, A. Rusconi, M. Savoia, A. Zamboni, J. A. Merrifield, E. K. Gibson, J. Carpenter, R. Fisackerly, B. Houdou, E. Sefton-Nash, and R. Trautner, “ProSPA: Analysis of lunar polar volatiles and isru demonstration on the moon.” *49th Lunar and Planetary Science Conference*, 2018.
- [5] D. Heather, E. Sefton-Nash, R. Fisackerly, R. Trautner, S. Barber, P. Reiss, D. Martin, and B. Houdou, “The esa prospect payload for luna 27: development status,” 03 2021.
- [6] J. Biswas, S. Sheridan, C. Pitcher, L. Richter, M. Reganaz, S. J. Barber, and P. Reiss, “Searching for potential ice-rich mining sites on the moon with the Lunar Volatiles Scout,” vol. 181, p. 104826, 2020.
- [7] P. Reiss, “A combined model of heat and mass transfer for the in situ extraction of volatile water from lunar regolith,” vol. 306, pp. 1–15, 2018.
- [8] M. J. Poston, G. A. Grieves, A. B. Aleksandrov, C. A. Hibbitts, M. D. Dyar, and T. M. Orlando, “Water interactions with micronized lunar surrogates JSC-1A and albite under ultra-high vacuum with application to lunar observations,” vol. 118, pp. 105–115, 2013.
- [9] S. L. Schroeder and M. Gottfried, “Temperature-programmed desorption, thermal desorption spectroscopy,” *Advanced Physical Chemistry Laboratory, FU Berlin*, 2002.
- [10] C. A. Hibbitts, G. A. Grieves, M. J. Poston, M. D. Dyar, A. B. Aleksandrov, M. A. Johnson, and T. M. Orlando, “Thermal stability of water and hydroxyl on the surface of the moon from temperature-programmed desorption measurements of lunar analog materials,” *ICARUS*, vol. 213, pp. 64–72, 2011.
- [11] D. R. Williams, “Moon fact sheet,” online, Jan. 2020. [Online]. Available: <https://nssdc.gsfc.nasa.gov/planetary/factsheet/moonfact.html>

- [12] K. A. Jackson, *Kinetic Processes: Crystal Growth, Diffusion, and Phase Transitions in Materials.* Wiley-VCH, 2010.
- [13] S. M. Clifford and D. Hillel, "Knudsen diffusion: the effect of small pore size and low gas pressure on gaseous transport in soil," *Soil Science*, vol. 141, no. 4, pp. 289–297, apr 1986.
- [14] R. Choate, S. A. Batterson, E. M. Christensen, R. E. Hutton, L. D. Jaffe, R. H. Jones, H. Y. Ko, R. L. Spencer, and F. B. Sperling, "Lunar surface mechanical properties," vol. 74, pp. 6149–6174, 1969.
- [15] H. A. Toutanji, S. Evans, and R. N. Grugel, "Performance of lunar sulfur concrete in lunar environments," vol. 29, pp. 444–448, 2012.
- [16] S. A. Reinecke and B. E. Sleep, "Knudsen diffusion, gas permeability, and water content in an unconsolidated porous medium," *Water Resources Research*, vol. 38, no. 12, pp. 16–1–16–15, dec 2002.
- [17] S. Parzinger, "Analytische Modellierung der temperatur- und gasdruckabhängigen effektiven Wärmeleitfähigkeit von Pulvern," Ph.D. dissertation, Technische Universität München, Institut für Energietechnik, Lehrstuhl für Thermodynamik, 2014.
- [18] H.-D. Vosteen and R. Schellschmidt, "Influence of temperature on thermal conductivity, thermal capacity and thermal diffusivity for different types of rock," vol. 28, pp. 499–509, 2003.
- [19] G. Zoth and R. Haenel, "Appendix. in: Haenel, r., stegena, l., rybach, l. (eds.), handbook of terrestrial heat-flow density determination," pp. 449–468, 1988.
- [20] M. A. Morris, M. Bowker, and D. A. King, "Chapter 1 kinetics of adsorption, desorption and diffusion at metal surfaces," pp. 1–179, 1984.
- [21] A. Griesinger, K. Spindler, and E. Hahne, "Measurements and theoretical modelling of the effective thermal conductivity of zeolites," *International Journal of Heat and Mass Transfer*, vol. 42, no. 23, pp. 4363–4374, dec 1999.
- [22] *VDI Heat Atlas.* Springer, 2010.
- [23] K. Swimm, G. Reichenauer, S. Vidi, and H.-P. Ebert, "Gas pressure dependence of the heat transport in porous solids with pores smaller than 10 μm ," vol. 30, pp. 1329–1342, 2009.
- [24] M. Reganaz, "Detailed design, assembly, integration, test and contamination assessment forthe LUVMI instrument," *Master Thesis, Technische Universität München*, 2018.
- [25] J. Biswas and M. Reganaz, "Volatiles sampler test report," TUM/OUN, Tech. Rep., 2018.

- [26] I. Martínez, "Radiative view factors," 1995. [Online]. Available: <http://webserver.dmt.upm.es/~isidoro/tc3/RadiationViewfactors.pdf>
- [27] I. Langmuir, "The adsorption of gases on plane surfaces of glass, mica and platinum." *J. Am. Chem. Soc.*, vol. 40, pp. 1361–1403, 1918.
- [28] N. Schorghofer and G. J. Taylor, "Subsurface migration of h₂o at lunar cold traps," *J. Geophys. Res.*, vol. 112, 2007.

Appendix A - Thermal Conductivity

This appendix presents a closer analysis of the influence of the two factors C_1 and C_2 of the solid conductance term k_s , see Eq. (2–22).

A total of six different combinations of the coefficients C_1 and C_2 have been analyzed, which can be found in Tab. 2–3. Figure A-1 shows the resulting thermal conductivity according to Eq. (2–19). For high temperatures all combinations reach similar values across the entire pressure range. At low temperatures however, a significant difference can be seen, especially for the combination $C_1 = 0.5, C_2 = 0.38$ the resulting conductivities at low pressures tend to be approximately two orders of magnitude lower than for every other combination. In the following figures, the respective ratios of the different mechanisms for each resulting thermal conductivity field of Fig. A-1 is presented.

Figure A-2 takes a closer look at the parts of the thermal conductivity resulting from the coefficients $C_1 = 0.5$ and $C_2 = 0.38$. The solid conductance term k_{sc} shown in the upper left dominates the low pressure low temperature region, but quickly falls off at $T \approx 200\text{ K}$ and $p \approx 1\text{ Pa}$. For higher temperatures the radiative part k_{rad} considerably increases in influence, due to the T^4 dependence of radiative heat transfer. Both k_{gas} and k_{sg} start to influence the magnitude of the thermal conductivity only at pressures above $p \approx 1\text{ Pa}$. The former generally is higher in the entire $T - p$ -domain.

The following figure, Fig. A-3 also shows the ratios of the thermal conductivity, this time resulting from the factors $C_1 = 474.0$ and $C_2 = 1.18$. As expected, higher coefficients for the Eq. (2–22) lead to higher values for the solid conductance. This change can be clearly seen in the top left graph, where the patches of $k_{sc}/k > 0.1$ visibly increased in size as compared to the previous figure. Subsequently, the radiative part of the thermal conductivity decreased, which can be seen especially in the high temperature domain. For both the gas and the solid-gas coupling conduction the ratios stayed approximately the same.

Figure A-4 features the results of the thermal conductivity following the next combination of the coefficients, $C_1 = 750.0$ and $C_2 = 0.75$. While the graphs are all similar to the ones from Fig. A-3, the ratio k_{sc}/k tends to decrease quicker with higher temperatures. To compensate this effect, the ratio k_{rad}/k generally increases quicker with increasing temperatures.

Results of the combinations $C_1 = 807.0$ and $C_2 = 0.64$, $C_1 = 1073.0$ and $C_2 = 0.13$, and $C_1 = 1293.0$ and $C_2 = 0.73$, are shown in Figs. A-3, A-6, and A-7, respectively. Though being rather similar, the differences between these three results can mainly be seen in the shape of the $k_{sc}/k = 0.1$ patch, which tends to increase its size into the high pressure and low temperature domain, as well as the retreating front of the $k_{rad}/k = 0.9$ patch, which vanishes completely for the last set of coefficients.

This analysis of the coefficients for the solid thermal conductance term k_s shows that the behavior of the heat transfer is greatly influenced by the choice of lunar soil and

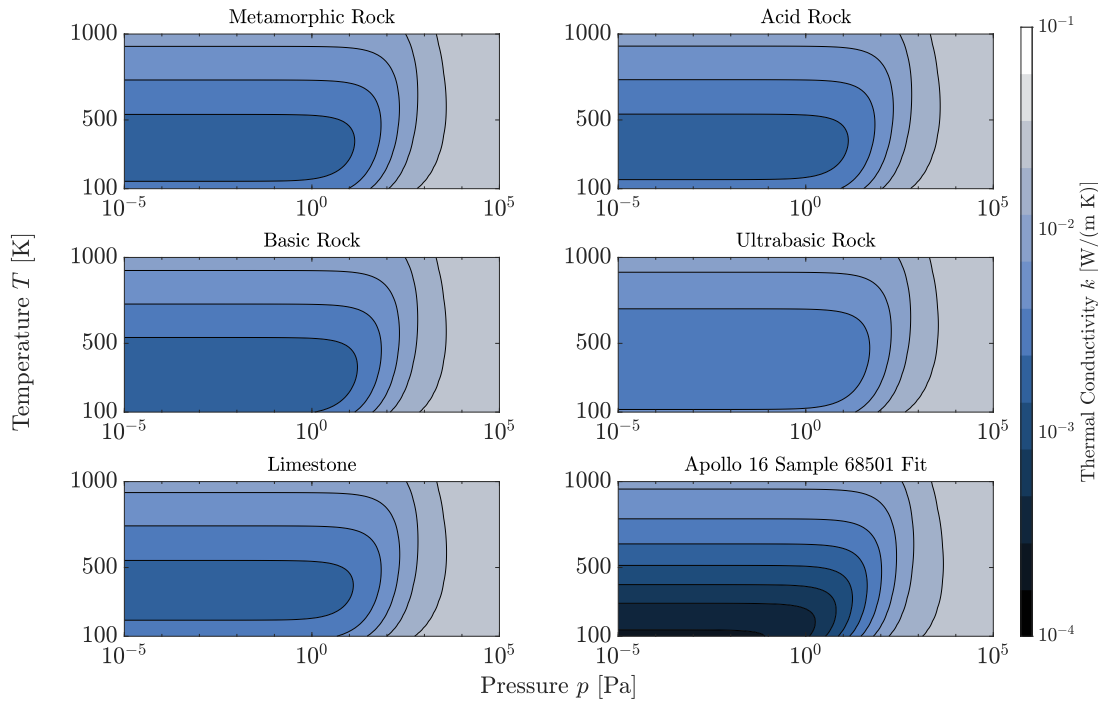


Fig. A-1: Comparison of the thermal conductivity as a result of changing factors C_1 and C_2 of the solid conductance term.

its respective set of coefficients C_1 and C_2 for the simulation. Especially at lower temperatures, where the solid conductivity generally dominates, the resulting thermal conductivity can differ by as much as two orders of magnitude. Since it is expected that higher values for k lead to a more evenly distributed temperature field, the thermal extraction of volatiles which depends on reaching certain threshold temperatures in order to properly desorb, is also greatly influenced.

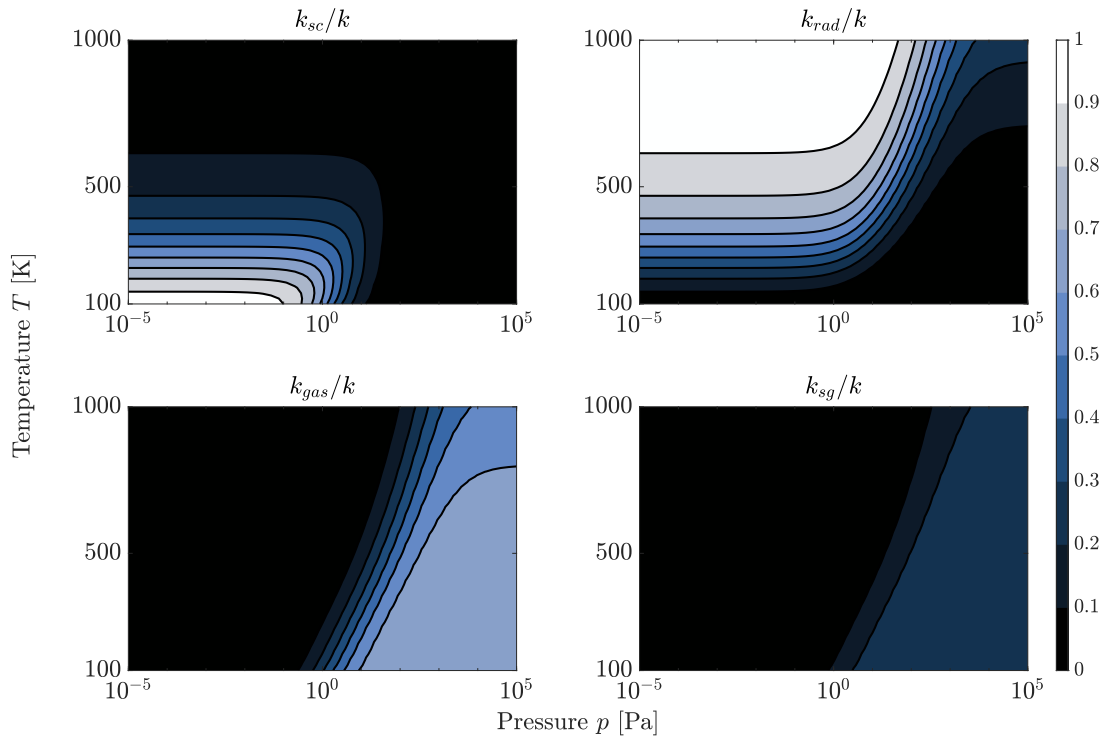


Fig. A-2: Ratios of the different components of the thermal conductivity for the factors $C_1 = 0.5$ and $C_2 = 0.38$.

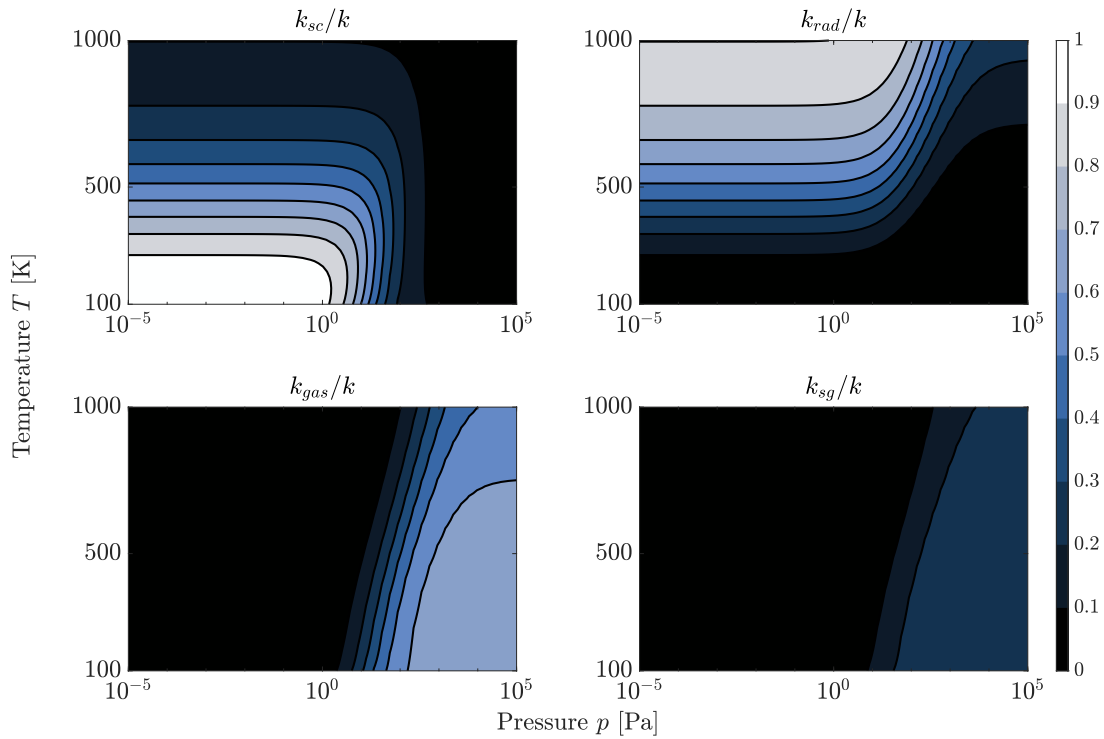


Fig. A-3: Ratios of the different components of the thermal conductivity for the factors $C_1 = 474$ and $C_2 = 1.18$.

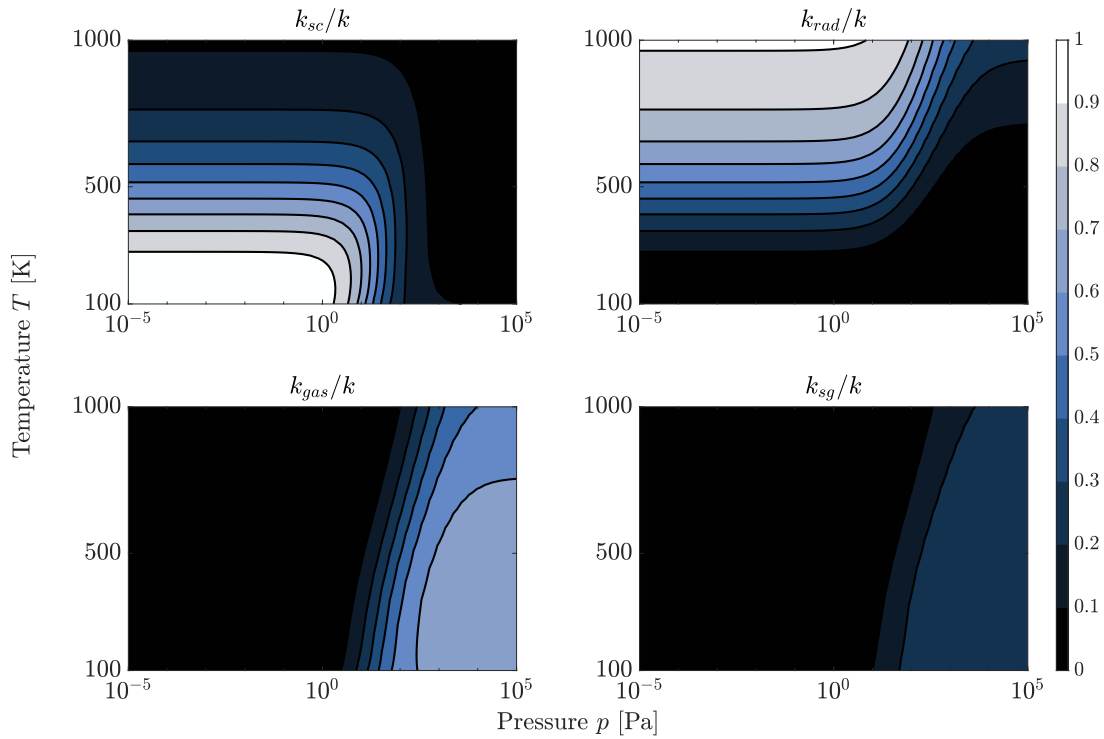


Fig. A-4: Ratios of the different components of the thermal conductivity for the factors $C_1 = 750$ and $C_2 = 0.75$.

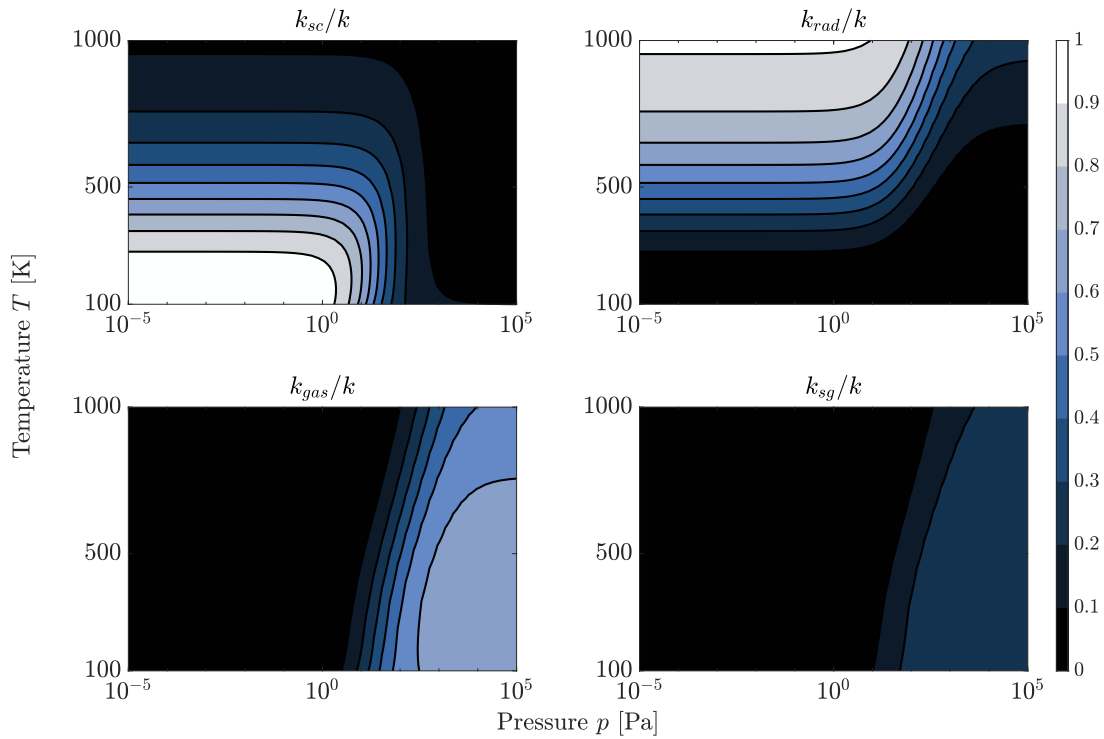


Fig. A-5: Ratios of the different components of the thermal conductivity for the factors $C_1 = 807$ and $C_2 = 0.64$.

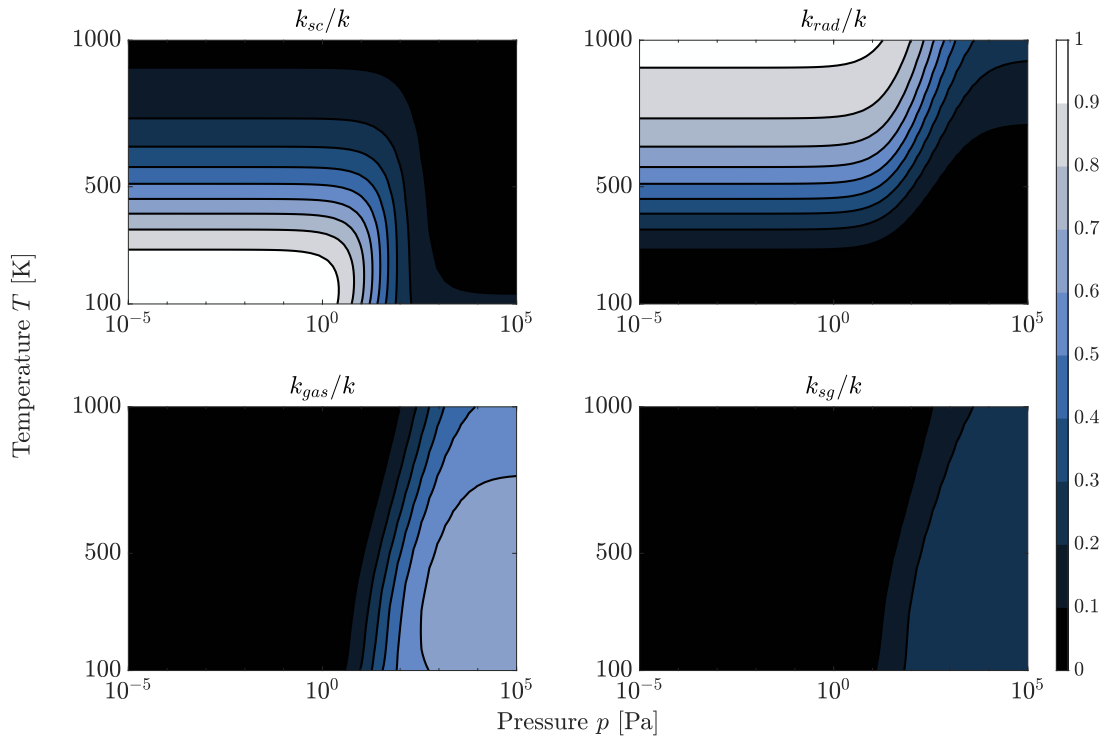


Fig. A-6: Ratios of the different components of the thermal conductivity for the factors $C_1 = 1073$ and $C_2 = 0.13$.

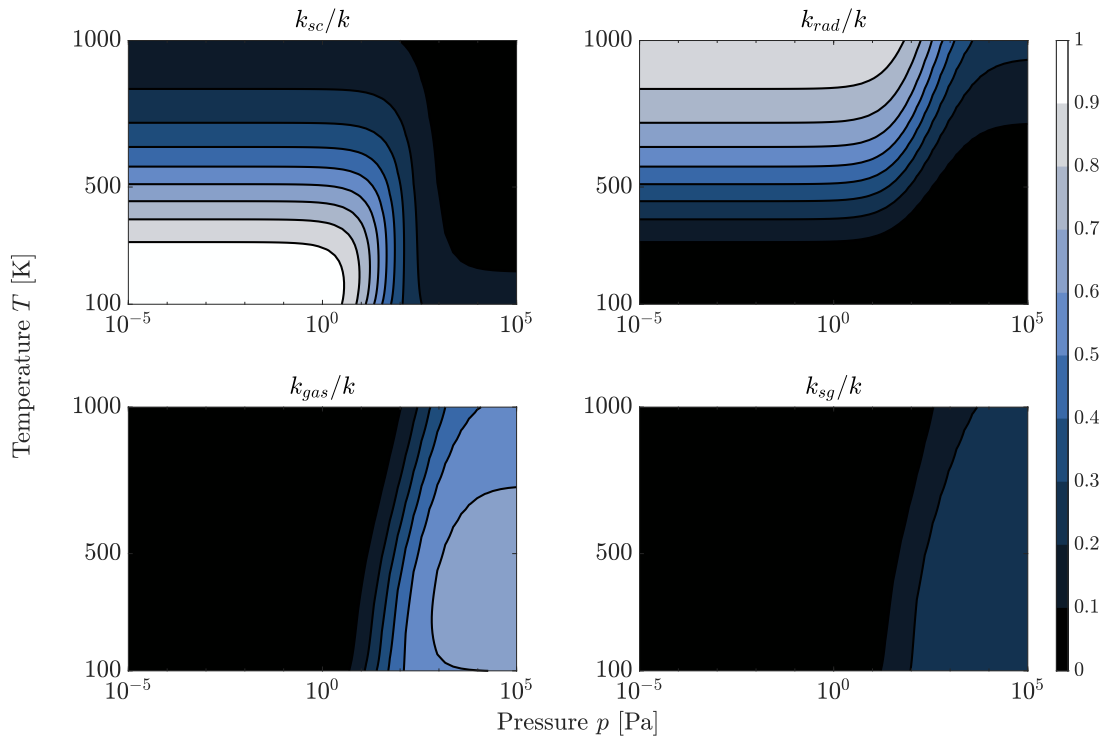


Fig. A-7: Ratios of the different components of the thermal conductivity for the factors $C_1 = 1293$ and $C_2 = 0.73$.

Appendix B - View Factors

The following equations were used to calculate the view factors of the faces inside of the enclosure of the inserted LVS [26].

$$F_{H \rightarrow DS} = 1 - \frac{1}{\pi} \left(\arccos \left(\frac{f_2}{f_1} \right) - \frac{f_4}{2h} \right) \quad (\text{B-1})$$

$$F_{H \rightarrow B} = 1 - F_{H \rightarrow DS} \quad (\text{B-2})$$

$$F_{DS \rightarrow DS} = 1 - \frac{1}{R} + \frac{2}{\pi R} \arctan \left(\frac{2\sqrt{R^2 - 1}}{h} \right) - \frac{hf_7}{2\pi R} \quad (\text{B-3})$$

$$F_{DS \rightarrow B} = 1 - F_{DS \rightarrow H} - F_{DS \rightarrow DS} \quad (\text{B-4})$$

with the surface of the heating rod (**H**), the drillshell (**DS**), and either the instrumentation or the lunar regolith considered as the base of the cylindrical enclosure (**B**). A sketch of the geometry can be seen in Fig. B-1. The remaining view factors can be calculated using the reciprocity rule, Eq. (B-5), or the summation rule, Eq. (B-6):

$$A_i \cdot F_{i \rightarrow j} = A_j \cdot F_{j \rightarrow i} \quad (\text{B-5})$$

$$\sum_{j=1}^N F_{i \rightarrow j} = 1. \quad (\text{B-6})$$

The view factors are governed by the geometry, which is represented in the two factors R and h :

$$R = \frac{R_2}{R_1} = \frac{R_{DS}}{R_H} \quad (\text{B-7})$$

$$h = \frac{H}{R_1} = \frac{H}{R_H} \quad (\text{B-8})$$

with the radii R_H of the outside heating rod, and R_{DS} of the inside of the drillshell, and the remaining height of the LVS sticking out of the regolith H . In order to keep the equations short, seven helping factors were introduced, f_1 to f_7 :

$$f_1 = h^2 + R^2 - 1 \quad (\text{B-9})$$

$$f_2 = h^2 - R^2 + 1 \quad (\text{B-10})$$

$$f_3 = \sqrt{(f_1 + 2)^2 - 4R^2} \quad (\text{B-11})$$

$$f_4 = f_3 \arccos \left(\frac{f_2}{Rf_1} \right) + f_2 \arcsin \left(\frac{1}{R} \right) - \frac{\pi f_1}{2} \quad (\text{B-12})$$

$$f_5 = \sqrt{\frac{4R^2}{h^2} + 1} \quad (\text{B-13})$$

$$f_6 = 1 - \frac{2h^2}{R^2(h^2 + 4R^2 - 4)} \quad (\text{B-14})$$

$$f_7 = f_5 \arcsin(f_6) - \arcsin \left(1 - \frac{1}{R^2} \right) + \frac{\pi}{2}(f_5 - 1). \quad (\text{B-15})$$

The resulting view factors for the problem depicted in Fig. B-1 using the equations above are shown in the Tab. B-1.

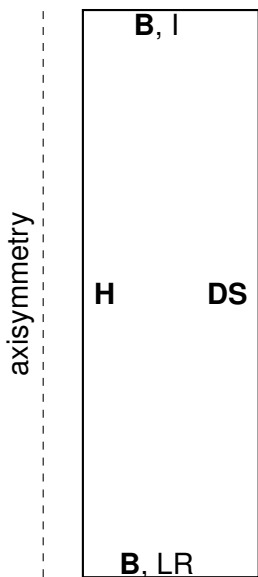


Fig. B-1: Sketch of the LVS enclosure.

Tab. B-1: Resulting view factors.

	Heater	DrillShell	Base, LR	Base, I
Heater	0.0	0.8012	0.0994	0.0994
DrillShell	0.1476	0.6006	0.1259	0.1259
Base, LR	0.0997	0.6860	0.0	0.2143
Base, I	0.0997	0.6860	0.2143	0.0

Appendix C - Resorption

This chapter includes an approach to describe the resorption process. The Langmuir Adsorption Theorem [27] states that the desorption and adsorption rate can be written as

$$r_d = k_d \cdot \Theta \quad (\text{C-1})$$

$$r_{ad} = k_{ad} \cdot p \cdot (1 - \Theta) \quad (\text{C-2})$$

so that the first time derivative of the surface coverage Θ is

$$\frac{d\Theta}{dt} = -r_d + r_{ad} \quad (\text{C-3})$$

with the pressure p . Since the surface coverage can be expressed as the fraction between the current adsorbed concentration c_a and the maximum adsorbed concentration c_{sat} , the equation can be multiplied by c_{sat} to get:

$$\frac{dc_a}{dt} = -k_d \cdot c_a + k_{ad} \cdot p \cdot (c_{sat} - c_a). \quad (\text{C-4})$$

At equilibrium conditions, the first time derivative is zero, which indicates that the two reaction rates are equal:

$$r_d|_{eq} = r_{ad}|_{eq} \quad (\text{C-5})$$

leading to:

$$\left. \frac{dc_a}{dt} \right|_{p=p_{eq}, c_a=c_{a,eq}} = 0 = -k_d \cdot c_{a,eq} + k_{ad} \cdot p_{eq} \cdot (c_{sat} - c_{a,eq}) \quad (\text{C-6})$$

$$\Rightarrow k_{ad} = k_d \cdot \frac{1}{p_{eq}} \cdot \frac{c_{a,eq}}{c_{sat} - c_{a,eq}} \quad (\text{C-7})$$

$$\Rightarrow \frac{dc_a}{dt} = -k_d \cdot c_a + k_d \cdot \frac{p}{p_{eq}} \cdot \frac{c_{sat} - c_a}{c_{sat} - c_{a,eq}} \cdot c_{a,eq}. \quad (\text{C-8})$$

This representation of the resorption process relies on the description of the equilibrium pressure p_{eq} as well as the equilibrium and saturation adsorbed species, $c_{a,eq}$ and c_{sat} respectively. The former can be approached by using equilibrium vapor pressure equations like the one from Schorghofer and Taylor [28]:

$$p_{eq} = p_t \exp \left(-\frac{Q}{R} \cdot \left(\frac{1}{T} - \frac{1}{T_t} \right) \right), \quad (\text{C-9})$$

which offers a temperature dependent description of the pressure, with $p_t = 611.657 \text{ Pa}$, $T_t = 273.16 \text{ K}$, and $Q = 51.058 \text{ J mol}^{-1}$. The saturation concentration can be assumed to be around 15wt.% [7], which leaves the description for the equilibrium adsorbed concentration. Similar to the equilibrium pressure it has to be a function of the temperature, which can be incorporated through the equilibrium pressure and the ideal gas law:

$$p_{eq} = \frac{c_{d,eq} \cdot R \cdot T}{\Phi} \Rightarrow c_{d,eq} = \frac{p_{eq} \cdot \Phi}{R \cdot T} \quad (\text{C-10})$$

which can be combined using the total sum of the concentrations

$$c = c_a + c_d = c_{a,eq} + c_{d,eq}. \quad (\text{C-11})$$

The final task is to implement limitations like $c_{a,eq} > 0 \text{ mol m}^{-3}$ and $0 \text{ mol m}^{-3} \leq c_a \leq c_{sat}$ in order to prevent negative adsorption or other unphysical behavior, which concludes the approach of the resorption process.